UCLA
UCLA Electronic Theses and Dissertations

Title

In the Investigation of New Materials/Structures and Their Applications in Energy Storage/Conversion Systems

Permalink

https://escholarship.org/uc/item/333438bm

Author

Zhong, Xing

Publication Date

2014

Peer reviewed|Thesis/dissertation

eScholarship.org Powered by the California Digital Library
University of California

UNIVERSITY OF CALIFORNIA

Los Angeles

In the Investigation of

New Materials/Structures and Their Applications

in Energy Storage/Conversion Systems

A dissertation submitted in partial satisfaction of the

requirements for the degree Doctor of Philosophy

in Chemistry

by

Xing Zhong

2014

© Copyright by

Xing Zhong

2014

ABSTRACT OF THE DISSERTATION

In the Investigation of

New Materials/Structures and Their Applications

in Energy Storage/Conversion Systems

by

Xing Zhong

Doctor of Philosophy in Chemistry

University of California, Los Angeles, 2014

Professor Xiangfeng Duan, Chair

As the need for energy is increasing fast these days, it is imperative to develop new and reliable energy conversion and storage technology strategies that are alternative to the fossil fuels. In the first part of my thesis, we investigate the possibility of utilizing silicon as potential photocatalyst in the organic waste degradation. We first demonstrate that the platinum nanoparticle loaded porous silicon nanowires can be used as effective photocatalysts for photocatalytic degradation of organic dyes and toxic pollutants under visible irradiation. Secondly, we demonstrate a facile and simple solution phase method to enhance and stabilize the photoactivity of silicon nanowires, by functionalizing the silicon nanowires with reduced graphene oxide sheets. Photocatalytic IC

dye degradation testing shows that the photoactivity of silicon nanowires can be enhanced and maintained without decay, featured with an initial activation process. In the second part of my thesis, we investigate various high energy density air battery systems. First of all, a silicon–air battery using an alkaline solution as electrolyte is investigated, achieving a high anode specific capacity. Second we demonstrate a new family of silicide based anode materials for high energy density primary air batteries. We show various silicide anodes (Mg_2Si, $TiSi_2$, $CoSi_2$ and VSi_2) can exhibit excellent electrochemical performance with unparalleled capacity in both thin film and bulk power pellet form. Lastly, we invent a hydrophobic three-dimensional (3D) graphene membrane as a moisture-resistive cathode for high performance Li-air batteries, enabling a robust Li-air battery with exceptional performance. All of these new technology strategies will open up exciting opportunities for many applications in the energy field.

The dissertation of Xing Zhong is approved.

Richard B. Kaner

Yu Huang

Xiangfeng Duan, Committee Chair

University of California, Los Angeles

2014

I dedicate this thesis to

my father Zhiwei Zhong, mother Wenjuan Pan

and my girlfriend Jiayi Yang

for their unconditional support and infinite love.

Table of Contents

List of Figures

Acknowledgments

First of all, I would like to thank my advisor, Professor Xiangfeng Duan, for guiding me throughout my Ph.D. study. I am very grateful that he devoted much of his time and energy to helping me develop academically and personally. I would also like to thank Professor Richard B. Kaner, Professor Yu Huang, Professor Craig A. Merlic for giving me invaluable advices in my dissertation. All of these have contributed to the accomplishment of my Ph.D. degree at UCLA. In addition, I would like to thank the collaborated group in Material Science and Engineering supervised by Professor Yu Huang. We shared experimental experiences, exchanged opinions on literatures and collaborated with each other. These help me quickly accumulate knowledge and experience in various fields in these years, which qualifies me as a Doctor of Philosophy. Additionally, I appreciate the collaboration with Dr. Min Xue and Professor Jeffrey I. Zink, BET support from Dr. Hiroyasu Furukawa and Professor Omar M. Yaghi.

VITA

2005-2009 B.S. in Chemistry, Nanjing University

2009-2011 M.S. in Chemistry, University of California, Los Angeles

Chapter 1 Introduction to Energy Conversion and Energy Storage

1.1 Energy Conversion

Exploring nanostructured materials for solar energy harvesting and conversion has attracted considerable attention due to its significant potential to address the ever-increasing challenges in renewable clean energy and environmental pollutions. Inorganic nanostructures such as nanoparticles, nanowires, nanotubes and nanosheets have been widely investigated for applications in next-generation photovoltaic devices. Alternatively, solar energy may also be harnessed, converted and stored as chemical energy using photocatalysts, in analogy to natural photosynthesis. For example, TiO_2 is one of the most widely used photocatalysts because of its exceptional stability towards chemical and photochemical corrosion. Previous investigations have recognized porous TiO_2 as a promising photocatalyst material for total destruction of common organic pollutants.[1-5] Unfortunately, the effective photoexcitation of TiO_2 has a large band gap of 3.2ev, and can only absorb 5% of solar energy.[6,7] Despite significant efforts to extend the absorption of TiO_2 systems towards longer wavelengths, the photocatalytic efficiency of TiO_2 in the visible light range still falls far from satisfactory. Recently, materials with a tunable band gap and strong absorption within visible light range such as silicon, many II-VI and III-V compounds, and other ternary compounds, have attracted great interest for solar energy harvesting. [8,9] For example, silicon based photoelectrodes and photocatalysts possess unique advantages, such as a favorable band gap of ~1.12 eV that enables absorption over the entire solar spectrum.[10-15] Developing new catalyst systems based on these alternative materials may open up a promising future for solar energy harvesting and conversion.

1.2 Energy Storage

High density electrochemical energy storage is of central importance for mobile power applications. The relatively low energy density and high cost associated with current approaches to electrochemical energy storage, including various battery and supercapacitor technologies, have been the main hurdle to its more widespread application. Amongst all battery technologies today, metal-air batteries have captured much attention recently due to their potential for very high energy densities.[16-18] For example, commercialized Zn-air batteries provide a practical energy density of ~350 Wh/kg out of a theoretical value of 1,370 Wh/kg.[19,20] The Zn-air system has several advantages over other metal-air batteries such as the low cost of raw materials, flat discharge profile and environmental benignity,[21,22] but is currently limited by relatively low energy density due to its large atomic weight. The Al-air system can provide a theoretical anode energy density of 8,100 Wh/kg,[23] but is perplexed by serious self-discharge.[24,25] The Li-air system, with an exceptionally high theoretical energy density of 13,000 Wh/kg, has also attracted considerable attention for its potential to provide an anode material with a projected energy density of ~1,700 Wh/kg.[26-28] However, the Li-air system can be limited by the scarcity, chemical instability and explosive hazard of the highly reactive elemental lithium. With a theoretical energy density of 8,470 Wh/kg, silicon-air batteries have recently been reported. [29] Additionally, other multi-electron materials such as metal borides and phosphides have also been investigated as potential candidates for high energy density anode materials,[30,31] but these materials often suffer from rather low open circuit voltages (with a theoretical maximum full cell voltage of 1.3 V and a demonstrated value of 0.87 V). Furthermore, the poor intrinsic conductivity of these materials can also limit the achievable power density of these systems and often requires additional conductive additives such as carbon black.

In my PhD thesis, I focus mainly on two parts: energy conversion (silicon based photocatalysts) and energy storage (new air battery systems). For the silicon based photocatalysts, we investigate the photocatalystic activity and stability by investigating silicon morphology and engineering hybrid structures. For the air battery systems, we investigate silicon-air battery, silicide-air battery, and Li-air battery and discuss their applications in both primary and secondary cells.

1.3 Bibliography

1. S. X. Li, F. Y. Zheng, X. L. Liu, F. Wu, N. S. Deng and J. H. Yang, *Chemosphere*, 2005, 61, 589-594.

2. C. Wang, J. Li, G. Mele, G. M. Yang, F. X. Zhang, L. Palmisano and G. Vasapollo, *Applied Catalysis B-Environmental*, 2007, 76, 218-226.

3. A. O. Ibhadon, G. M. Greenway, Y. Yue, P. Falaras and D. Tsoukleris, *Applied Catalysis B-Environmental*, 2008, 84, 351-355.

4. J. K. Liu, T. C. An, G. Y. Li, N. Z. Bao, G. Y. Sheng and J. M. Fu, *Microporous and Mesoporous Materials*, 2009, 124, 197-203.

5. G. S. Shao, F. Y. Wang, T. Z. Ren, Y. P. Liu and Z. Y. Yuan, *Applied Catalysis B-Environmental*, 2009, 92, 61-67.

6. K. H. Yoo, K. S. Kang, Y. Chen, K. J. Han and J. Kim, *Nanotechnology*, 2008, *19*, 505202.

7. H. J. Zhang, G. H. Chen and D. W. Bahnemann, *Journal of Materials Chemistry*, 2009, 19, 5089-5121.

8. Y. Q. Qu, X. F. Duan, *Chem. Soc. Rev.* 2013, 42, 2568-2580.

9. Y. Li, F. Qian, J. Xiang, C. M. Lieber, *Materials Today,* 2006, 9, 18.

10. Q. Qing, S. K. Pal, B. Z. Tian, X. J. Duan, B. P. Timko, T. Cohen-Karni, V. N. Murthy, C. M.

Lieber, *Proc. Natl. Acad. Sci. U. S. A.* 2010, 107, 1882-1887.

11. I. Oh, J. Kye, S. Hwang, *Nano Lett.* 2012, 12, 298-302.

12. G. M. Wang, Y. C. Ling, Y. Li, *Nanoscale* 2012, 4, 6682-6691.

13. G. M. Wang, Y. C. Ling, H. Y. Wang, X. H. Lu, Y. Li, *Journal of Photochemistry and Photobiology C: Photochemistry Reviews* 2014, 19, 35-51.

14. H. L. Zhou, Y. Q. Qu, T. Zeid, X. F. Duan, *Energy Environ. Sci.* 2012, 5, 6732-6743.

15. Y. Q. Qu, X. F. Duan, *J. Mater. Chem.* 2012, *22*, 16171-16181.

16. S. Xu, Y. Qin, C. Xu, Y. G. Wei, R. Yang, Z. L. Wang, *Nat. Nanotech*. 2010, 5, 366-373.

17. B. Tian, X. L. Zheng, T. J. Kempa, Y. Fang, N. F. Yu, G. Yu, J. Huang, C. M. Lieber, *Natur*e., 2007, 449, 885-888.

18. A. I. Hochbaum, P. D. Yang, Chem. Rev. 2010, 110, 527-546.

19. G. Girishkumar, B. McCloskey, A. C. Luntz, S. Swanson, W. Wilcke, *J. Phys. Chem. Lett*., 2010, 1, 2193-2203.

20. http://data.energizer.com/PDFs/alkzincairnomercury_psds.pdf

21. C. Chakkaravarthy, A. K. A. Waheed, H. V. K. Udupa,. *J. Power Sources,* 1981, 6, 203-228.

22. V. Neburchilov, H. J. Wang, J. J. Martin, W. Qu, *J. Power Sources,* 2010, 195, 1271-1291.

23. Y. Hori, J. Takao, H. Shomon, *Electrochim. Acta*., 1985, 30, 1121.

24. C. S. Li, W. Q. Ji, J. Chen, Z. L. Tao, *Chem. Mater.,* 2007, 19, 5812 – 5814.

25. http://www.altekfuel.com/userfiles/File/SDS_APS100_12-24_V-04.pdf

26. P. G. Bruce, L. J. Hardwick, K. M. Abraham, *MRS Bull.,* 2011, 36, 506-512.

27. P. G. Bruce, S. A. Freunberger, L. J. Hardwick, J. M. Tarascon, *Nat. Mater.,* 2012, 11, 19-29.

28. J. Christensen, P. Albertus, R. S. Sanchez-Carrera, T. Lohmann, B. Kozinsky, R. Liedtke, J.

Ahmed, A. Kojic, *J. Electrochem. Soc*., 2012, 159, R1-R30.

29. G. Cohn, D. Starosvetsky, R. Hagiwara, D. D. Macdonald, Y. Ein-Eli, *Electrochem. Commun.*, 2009, 11, 1916-1918.

30. H. X. Yang, Y. D. Wang, X. P. Ai, C. S. Cha, *Electrochem. Solid-State Lett.*, 2004, 7, A212-A215.

31. S. Licht, H. M. Wu, X. W. Yu, Y. F. Wang, *Chem. Commun.*, 2008, 28, 3257-3259.

Chapter 2 Photocatalytic Properties of Porous Silicon Nanowires

2.1 Introduction

Porous materials have attracted considerable interest due to the potential applications in broad areas including catalysis, integrated optics, energy harvesting and biotechnology.[1-6] For example, porous materials are widely used as supports for catalysts because of the abundant pores, large surface areas and the ease of recycling compared to nanopowders. Recently, porous materials have also been regarded as a promising candidate in solar energy harvesting with the development of synthetic routes to new types of porous materials, especially porous TiO_2.[1,7-15] However, the effective photoexcitation of TiO_2 requires the irradiation in the ultraviolet (UV) region due to its large band gap (3.2eV), which leads to a merely 5% of solar energy absorption.[16,17] Considerable efforts have been devoted to improving TiO_2 photocatalytic performances in the visible light range. Such efforts include nitrogen, phosphate or fluorine doping, transition metal ions doping and surface modification with dyes or quantum dots.[11-15,18-25] However, significant challenges remain to render the absorption of the modified TiO_2 materials spanning across the entire visible light range.

Recently, synthetic approaches toward single crystal porous silicon nanowires (SiNWs)[26,27] have been developed. Such nanowires are obtained through a metal-assisted electroless wet chemical etching approach, and exhibit a broad visible emission centered around 650 nm. The emission in the visible range could be attributed the deep quantum confinement and/or complex surface electronic states in the porous SiNWs. These studies suggest excitons generated within the porous SiNWs could be energetic enough to drive applicable photoelectrochemical reactions.[26,28] Compared to TiO_2, the overall absorption of

the porous SiNWs is much broader as it spans over the entire spectral range from UV to visible and near infrared (IR). In this study, we show that platinum nanoparticles (PtNPs) can be loaded onto porous SiNWs with controlled density amd demonstrate that the porous SiNWs and the PtNP loaded porous SiNWs can be used as effective photocatalysts for the photodegradation of indigo carmine (IC) and 4-nitrophenol (4NP) with visible light.

2.2 Results and Discussion

Microstructure characterizations of the porous SiNWs were summarized in Figure 2.1 SEM image shows high density vertical array of well-aligned porous SiNWs can be readily achieved with the diameters on the order of 100 nm and length on the order of 10 mm (Figure 2.1(a)). The TEM image clearly shows porous structure of the resulting SiNWs (Figure 2.1(b)).

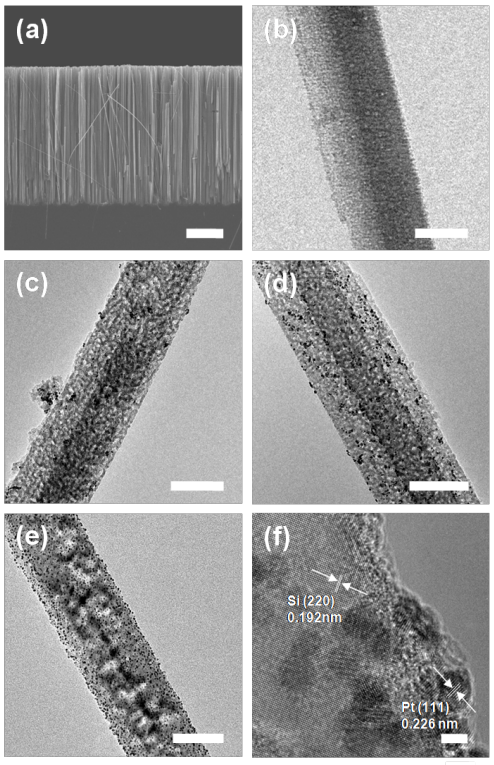

Figure 2.1 Characterization of the porous SiNWs and PtNP loaded porous SiNWs. (a) SEM image of the cross section of the as-etched porous SiNWs. (b) TEM image of a typical porous SiNW. (c) TEM image of the PtNP-pSiNW-A. (d) TEM image of the PtNP-pSiNW-B. (e) TEM image of the PtNP-pSiNW-C. (f) HRTEM image of the PtNP-pSiNW-C. The scale bar is 10 μm for A, 2 nm for F, and 100 nm for all others.

Incorporating selected metal nanoparticles onto semiconductor photocatalysts can enhance the photocatalytic activity because the difference in their Fermi levels can introduce a Schottky barrier between the metal and the semiconductor.[16] The built-in potential within the Schottky barrier can facilitate the separation of photogenerated electron-hole pairs. Futhermore, properly selected metal nanoparticles can also function as the catalysts to facilitate certain redox reactions. To this end, we have prepared PtNPs and loaded them onto the porous SiNWs. Specifically, PtNPs with 3-4 nm diameters were synthesized using poly(vinylpyrrolidone) (PVP) as the capping ligands[29]. The as-synthesized PtNPs typically have negative surface charges originated from PVP ligands, and cannot be readily attached onto porous SiNWs that also have negative surface charges. To facilitate the attachment of PtNPs onto porous SiNWs with sufficient yield, the porous SiNWs were functionalized with APTMS to render positively charged surface. The PtNPs can then be loaded onto functionalized porous SiNWs through electrostatic force. Controlled densities of PtNPs on porous silicon nanowires were achieved by adding various amounts of PtNPs into a fixed volume of porous SiNW suspension. It should be noted that density of PtNPs enventually saturates and reach an adsorption/desorption equilibrium when the positive surface charges on porous SiNWs are mostly compensated by the negative charges on PtNPs. In this way, we have prepared three photocatalyst samples with variable densities of PtNPs by adding 250 μL,

500 μL and 1000 μL of PtNP solution into 2 ml of ethanol dispersion containing 3.0 mg porous SiNWs, and named the these samples as PtNP-pSiNW-A, PtNP-pSiNW-B and PtNP-pSiNW-C, respectively. TEM studies clearly show that PtNPs are well anchored on the porous SiNWs with increasing densities (Figure 2.1(c-e)). The HRTEM image further illustrates good conjugation between the PtNPs and the porous SiNWs (Figure 2.1(f)).

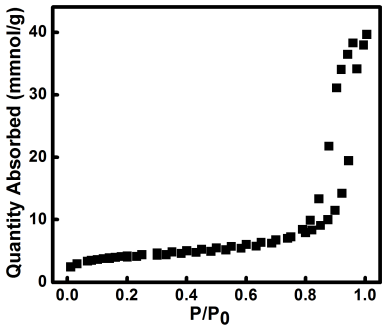

Figure 2.2 Typical nitrogen adsorption/desorption isotherms of the porous SiNWs

Nitrogen gas adsorption/desorption isotherm measurements were used to determine surface areas, average pore size and pore volume of the porous SiNWs. The porous SiNWs, which were prepared by immersing the wafer in an etching solution containing 0.3 M H_2O_2 and 4.8 M HF for 60 minutes were carefully scratched off from half of a 4-inch wafer with a razor blade. The mass of the porous SiNWs was determined after the samples were degassed overnight at 250 °C. A typical adsorption/desorption isotherm for 20.1 mg of the collected porous SiNWs is shown in Figure 2.2. The standard multipoint Brunauer-Emmett-Teller (BET) analysis of the porous SiNWs yields an exceptionally high surface area of 337 $m^2 \cdot g^{-1}$, which is comparable to the recently reported p-type mesoporous silicon nanowires (342 $m^2 \cdot g^{-1}$) [26] and mesoporous TiO_2 nanostructures (50 - 300 $m^2 \cdot g^{-1}$).[11-15] An average pore diameter of 14.0 nm is calculated based on the Barret-Joyner-Halenda (BJH) model. The total pore volume is 1.184 cm^3/g at $P/P^o = 0.97$ for the porous SiNWs. The high surface area and

large pore volume suggest that the semiconducting porous SiNWs will be a peculiar and promising material for energy harvesting and photocatalysis purposes.

Traditional metal oxide photocatlysts such as TiO_2 and ZnO only absorb a small portion of the solar spectrum because of their large band gaps. Significantly, our study shows the absorption spectrum of the porous SiNWs spans across the entire UV, visible light and near IR range (Figure 2.3(a)). Therefore, the photocatalytic reactions based on porous silicon nanostructures could be effectively carried out under visible light or even under near IR light. To evaluate the photocatalytic activity of the porous SiNWs, two sets of experiments were carried out for the photodegradation of indigo carmine (IC) and 4-nitrophenol (4NP).

Under light irradiation, the electron-hole pairs are generated in the porous-SiNWs and then separated, which further react with the dissolved O_2 and water to produce reactive oxygen species (ROS) such as hydroxyl radicals ($OH^{\bullet}$), superoxide ($O_2^{\bullet -}$), singlet oxygen ($^1O_2$), and peroxide (H_2O_2). ROS are strong oxidants and known as nonselective oxidizing agents for organic pollutants.[30] They can oxidize IC into CO_2, H_2O, HNO_3 and sodium sulfate. The reactions are listed as follows:

Porous silicon nanowires $\xrightarrow{h\nu}$ $h^+ + e^-$

Conduction band: $O_2 + 4H^+ + 4e^- \rightarrow 2H_2O$

Valence band: $h^+ + H_2O \rightarrow$ ROS $+ H^+$

ROS + indigo carmine $\rightarrow$ intermediates $\rightarrow$ $CO_2 + H_2O + HNO_3$ + sodium sulfate

The photodegradation of IC was carried out in a photocatalyst dispersion of 0.3 mg/ml under the irradiation of a 300 W xenon light. The change of IC concentration ([IC]) is monitored as a function of reation time. When the fresh photocatalyst sample PtNP-pSiNW-C

was used in the reaction, the change of the [IC] clearly shows three distinct reaction stages: slower reaction rate at the beginning (12.2% degraded IC within 15 minutes), faster reaction rate in the middle (70.3% degraded IC within the subsequent 45 minutes), and slower reaction rate again in the end. The initial slower reaction rate could be attributed to the simultaneous photodegradation of IC and other absorbed organic species including PVP ligand on PtNP surfaces. After 30 minutes when PVP and other absorbed organic molecules were exhausted, the change of [IC] could be greater than that at the initial stage. When the [IC] dropped to a very low concentration, the ROS have a lower probability to be captured by the IC molecules, leading to a slower degradation rate.

To remove this initial slow reaction stage and more accurately estimate the catalytic activity of various PtNP-pSiNW photocatalysts, all catalyst samples were exposed to light irradiation for 1 hour before photodegradation of IC and 4NP. The photocatalytic activity of the four catalysts on the degradation of IC is compared in Figure 2.3(b). After 60 minutes of irradiation, the percentages of degraded IC are 37.2%, 51.1%, 62.2% and 86.9% for porous SiNWs, PtNP-pSiNW-A, PtNP-pSiNW-B and PtNP-pSiNW-C, respectively. In contrast, only 4.7 % of IC molecules were degraded with the same irradiation conditions without the PtNP-pSiNW photocatalysts. Our results clearly demonstrate that porous SiNWs can function as effective photocatalysts in the visible irradiation range and that the Pt-loaded porous SiNWs are much more efficient photocatalysts than the porous SiNWs only. This catalytic enhancement by PtNPs could be attributed be their ability to facilitate electron-hole separation and to promote electron transfer process in catalytic photodegradation reaction.

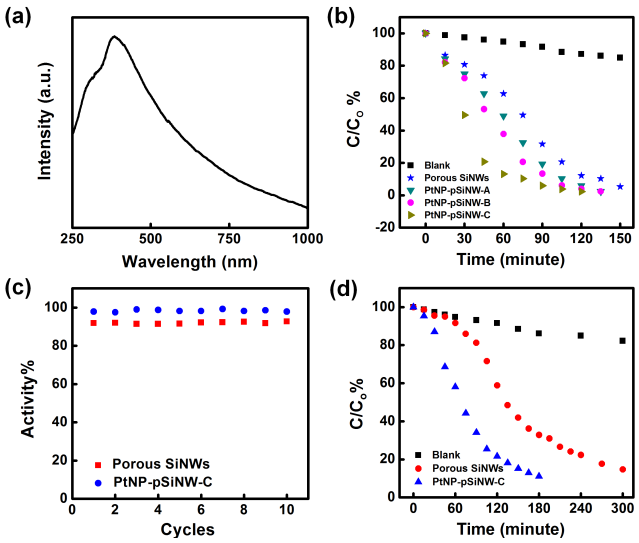

Figure 2.3 Photocatalytic properties of the porous SiNWs and Pt loaded porous SiNWs. (a) Absorption spectrum of the porous SiNWs. The concentration of porous SiNWs was set at 0.1 mg/ml. (b) IC degradation catalyzed by the porous SiNWs and Pt loaded porous SiNWs. Black squares represent the IC under the light irradiation without photocatalysts. Blue stars, dark cyan down-triangles, magenta circles and dark yellow right-triangles represent the catalytic behaviour of the porous SiNWs, PtNP-pSiNW-A, PtNP-pSiNW-B and PtNP-pSiNW-C, respectively. The concentration of all catalysts was set at 0.3 mg/ml. (c) Photocatalytic stability of the porous SiNWs and PtNP-pSiNW-C. Red squares and blue circles represent the catalytic behaviors of the porous SiNWs and the PtNP-pSiNW-C, respectively. The activity of each photocatalyst is represented by the percentage of IC degraded in a given reaction. (d) 4NP degradation catalyzed by the porous SiNWs and PtNP loaded porous SiNWs. Black squares represent the 4NP without photocatalysts. Red circles and blue up-triangles represent the catalytic behaviors of the porous SiNWs and the PtNP-pSiNW-C, respectively.

It is imporant to compare the photocatalytic activity of the porous SiNW samples with more commonly used TiO_2 nanoparticles. To this end, we have carried out a sesries control experiments using 5 nm anatase TiO_2 nanoparticles[31] and P25 TiO_2 nanoparticles under same conditions with same weight concentration. Under visible light, our studies show that porous

SiNWs show photocatalyctic activity higher than anatase TiO_2 nanoparticles but lower than P25 TiO_2 nanoparticles. This difference can be largely attributed to the absorption properties of these three samples, with the P25 TiO_2 nanoparticles show largest overall absoprtion, and porous SiNWs next, and anatase TiO_2 nanoparticles least. Despite a band gap in the visible range (1.4-2.5 eV), the relatively low absorption of porous SiNWs may be attributed to the low intrinsic absorption coefficient of silicon compared to TiO_2.[32,33] In the IR regime, the porous SiNWs show best absorption and best photocatalytic activity among three photocatalysts. In addition to the band gap and absoprtion properties, it should be noted that the relative alignment of the conduction and valence band edge vs. redox potentials may also affect the photocatalytic activity. Future studies to determine the relative band edge alignment of porous SiNWs and its impact on the photocatalytic activity may offer clues for additonal improvement. .

The photocatalytic stability of the porous SiNWs was also evaluated by recycling the porous SiNWs for multiple cycles of reactions (red squares, in Figure 2.3(c)). The concentration of the catalysts was controlled at 0.3 mg/mL in 100 μM IC solution. After 2.5 hours of light irradiation, the catalysts were recovered by centrifugation and redispersed in a fresh IC solution for the next cycle of test. The catalysts show stable photocatalytic behavior after 10 cycles of reactions, demonstrating the high photostability of the porous SiNWs. A similar experiment was carried out to test the life time of the PtNP-pSiNW-C sample (blue circles in Figure 2.3(c)). The mixture was exposed under the light irradiation for 90 minutes with near complete IC degradation for each cycle. The PtNP-pSiNW-C catalyst also showed similar photocatalytic stability.

Photocatalyst is of significant interest in photodegradation of organic pollutant for waste

treatment in environment. For example, ROS can oxidize 4-nitrophenol (4NP) into CO_2 and H_2O. To this end, we have explored the porous SiNWs and PtNP-pSiNW-C as the photocatalysts to degrade 4NP to evaluate their photocatalytic ability in organic waste treatment (Figure 2.3(d)). 18.8 % and 66.0% of the 4NP were degraded after 90 minutes of light irradiation with the porous SiNWs and the PtNP-pSiNW-C, respectively. The results further demonstrate the photocatalytic ability of the porous SiNWs in degrade organic species and confirm that PtNP loading can promote photocatalytic activity. Reactions with the catalysts exposed to xenon light for 1 hour also show a catalytic behavior with an initial slow degradation rate followed by a faster and then another slow reaction rate. This could be attributed to the variable amount of 4NP molecules absorbed on the surface of the porous SiNWs, which determines the degradation rate. Previous studies on the photodegradation of 4NP catalyzed by TiO_2 particles show that the amount of absorbed 4NP molecules on the catalysts is related to the pH values: a lower pH value often leads to higher 4NP molecules absorption.[11] The optimal pH for 4NP absorption on TiO_2 surface is 4.0. In the case of porous SiNWs, a thin layer of silicon oxide forms on the surface with abundant $(SiO)_3Si–OH$ groups.[34,35] The pKa of such silica surface is 4.5,[36] similar to that of the TiO_2 surface (pKa~4.95).[37] In porous SiNWs catalyzed photodegradation of 4NP, the starting solution has a pH value of 7.18 due to the pK_a value of 7.08 for 4NP. The initial amount of the absorbed 4NP molecules is limited by this pH value. As the reaction proceeds, CO_2 and HNO_3 are generated, which reduces the pH value of the reaction solution to 5.71 after 60 minute reaction. The lower pH value favors the adsorption of 4NP molecules on the catalysts and thus accelerates the degradation rate. The slow reaction rate at the final stage could be attributed to the lower concentration of 4NP in the reaction solution. Compared to the porous

SiNWs, reactions involving the PtNP-pSiNW-C catalysts display a shorter period of the initial slower stage because the PtNPs accelerate the degradation reaction and lead to a lower pH value within a shorter time duration.

2.3 Conclusions

In conclusion, we have shown that porous SiNWs can be synthesized with a large surface area (337 $m^2 \cdot g^{-1}$) and broad spectrum absorption throughout the entire spectral regime from UV to near IR range. We have further shown that PtNPs can be loaded onto porous SiNWs with controllable density. The combined advancements allow us to explore porous SiNWs as efficient and stable photocatalysts for the photodegradation of organic dyes such as IC and toxic pollutants such as 4NP, which may have significant interest for organic waste treatment and environmental remediation.

2.4 Materials and Method

Synthesis of Porous Silicon Nanowires. Porous SiNW arrays were synthesized through a two-step method involving the deposition of silver particles on the bare silicon surface followed by wet chemical etching. Briefly, pieces of the commercially available n-type Si (100) wafers with resistivity of 0.008 – 0.02 Ω·cm were used as the starting materials. The silicon pieces were cleaned by sonication in acetone and isopropanol and dried by nitrogen blow. The cleaned silicon pieces were immersed into a buffered oxide etchant (BOE) for 2 minutes to remove the native oxide layer and then immediately soaked into a solution containing 0.005 M $AgNO_3$ and 4.8 M HF for 1 minute at room temperature. The color of the Si surface turned from dark to colorful, indicating the formation of silver nanoparticles on surface. The silver-deposited Si pieces were rinsed with de-ionized water to remove extra silver ions and then immediately

immersed into an etching bath containing 4.8 M HF and 0.3 M H_2O_2 for 60 minutes. The silver metal was removed from the nanowires by immersing the Si pieces into the concentrated nitric acid for an hour.

Synthesis of Platinum Nanoparticles. For the synthesis of PtNPs, 0.05 mmol of K_2PtCl_4 and 1 mmol of poly(vinylpyrrolidone) (in terms of repeating units) were dissolved in 10 ml of ethylene glycol in a round bottom flask at room temperature.[29] The mixture was heated to 180 °C for 30 min with vigorous magnetic stirring. The solution was naturally cooled down to room temperature and 40 ml of acetone was added to precipitate out the PtNPs that were collected by centrifugation at 5000 rpm. The collected PtNPs were then re-dispersed in 5 ml of ethanol and precipitated out by 45 ml of hexane. The process was repeated for three times to thoroughly wash the nanoparticles. The final PtNPs were dissolved in 10 ml of ethanol for characterization and subsequent reactions.

Formation of Pt loaded Porous Silicon Nanowires. The porous SiNWs were first treated with aminopropyl-trimethoxy silane (APTMS). Typically, 3 mg of porous SiNWs were dispersed in 10 ml of 1% APTMS in ethanol. The mixture was refluxed for 2 hours and then centrifuged and washed with ethanol for three times. The APTMS modified porous SiNWs were re-dispersed in 5 ml of ethanol and mixed with various amount of PtNPs for 2 hours under vigorous stirring. The product was centrifuged and washed with ethanol for three times. The Pt loaded porous SiNWs were dried under vacuum for 2 hours.

Characterization of the Porous Silicon Nanowires. The as-etched samples were inspected with a scanning electron microscope (SEM) (JEOL 6700) at 10 kV of electron acceleration voltage. Transmission electron microscopy (TEM) imaging of the porous SiNWs and the PtNP loaded porous SiNWs was conducted on Phillips CM120 with a 120 kV operation voltage. The high

resolution TEM (HRTEM) were collected on FEI Titan with a 300 kV operation voltage. The surface area was measured by the BET method using a Micromeritics ASAP 2020 apparatus (Micromeritics, Norcross, GA). Multipoint isotherms in the P/P^o relative pressure range of 0.01 – 1.0 were measured by nitrogen adsorption at 77K. The sample was degassed overnight at 250 °C before the BET measurements.

Photocatalytic Ability of Porous Silicon Nanowires. Indigo carmine (IC) photocatalytic degradation reaction was carried out using 0.3 mg/mL of the porous SiNWs or PtNP-pSiNW dispersed in 100 μM of IC aqueous solution. The mixture was irradiated under a 300 W xenon lamp. The photocatalytic reaction was carried out in a glass container so that the UV portion of the Xe light is significantly reduced by glass absorption. The IC degradation was monitored by a Beckman DU-800 UV-vis spectrophotometer. The degradation of 4-nitrophenol (4NP) was performed with the same procedure as the IC degradation. The concentration of 4NP was determined by UV-vis spectrophotometer. All photocatalytic reactions were carried out under ambient conditions. The reaction system was cooled by strong air blowing, with he temperature of solution kept below 35 °C during the measurments.

2.5 Bibliography

1. M. E. Davis, *Nature*, 2002, 417, 813-821.
2. C. Sanchez, B. Lebeau, F. Chaput, J. P. Boilot, *Advanced Materials*, 2003, 15, 1969-1994.
3. M. H. Bartl, S. W. Boettcher, K. L. Frindell, G. D. Stucky, *Accounts of Chemical Research*, 2005, 38, 263-271.
4. A. M. Seayad, D. M. Antonelli, *Advanced Materials*, 2004, 16, 765-777.
5. A. Taguchi, F. Schuth, *Microporous and Mesoporous Materials*, 2005, 77, 1-45.

6. Slowing, II, J. L. Vivero-Escoto, C. W. Wu, V. S. Y. Lin, *Advanced Drug Delivery Reviews*, 2008, 60, 1278-1288.

7. A. Hagfeldt, M. Gratzel, *Accounts of Chemical Research*, 2000, 33, 269-277.

8. M. Zukalova, A. Zukal, L. Kavan, M. K. Nazeeruddin, P. Liska, M. Gratzel, *Nano Letters*, 2005, 5, 1789-1792.

9. S. W. Boettcher, J. Fan, C. K. Tsung, Q. H. Shi, G. D. Stucky, *Accounts of Chemical Research*, 2007, 40, 784-792.

10. K. M. Coakley, M. D. McGehee, *Applied Physics Letters*, 2003, 83, 3380-3382.

11. S. X. Li, F. Y. Zheng, X. L. Liu, F. Wu, N. S. Deng, J. H. Yang, *Chemosphere*, 2005, 61, 589-594.

12. C. Wang, J. Li, G. Mele, G. M. Yang, F. X. Zhang, L. Palmisano, G. Vasapollo, *Applied Catalysis B-Environmental*, 2007, 76, 218-226.

13. A. O. Ibhadon, G. M. Greenway, Y. Yue, P. Falaras, D. Tsoukleris, *Applied Catalysis B-Environmental*, 2008, 84, 351-355.

14. J. K. Liu, T. C. An, G. Y. Li, N. Z. Bao, G. Y. Sheng, J. M. Fu, *Microporous and Mesoporous Materials*, 2009, 124, 197-203.

15. G. S. Shao, F. Y. Wang, T. Z. Ren, Y. P. Liu, Z. Y. Yuan, *Applied Catalysis B-Environmental*, 2009, 92, 61-67.

16. K. H. Yoo, K. S. Kang, Y. Chen, K. J. Han, J. Kim, *Nanotechnology*, 2008, *19*, 505202.

17. H. J. Zhang, G. H. Chen, D. W. Bahnemann, *Journal of Materials Chemistry*, 2009, 19, 5089-5121.

18. S. Rodrigues, K. T. Ranjit, S. Uma, I. N. Martyanov, K. J. Klabunde, *Advanced Materials*, 2005, 17, 2467-2471

19. P. N. Kapoor, S. Uma, S. Rodriguez, K. J. Klabunde, *Journal of Molecular Catalysis a-Chemical*, 2005, 229, 145-150.

20. S. Usseglio, A. Damin, D. Scarano, S. Bordiga, A. Zecchina, C. Lamberti, *Journal of the American Chemical Society*, 2007, 129, 2822-2828

21. H. M. Luo, T. Takata, Y. G. Lee, J. F. Zhao, K. Domen, Y. S. Yan, *Chemistry of Materials*, 2004, 16, 846-849.

22. D. Chatterjee, S. Dasgupta, *Journal of Photochemistry and Photobiology C-Photochemistry Reviews*, 2005, 6, 186-205.

23. C. Ratanatawanate, Y. Tao, K. J. Balkus, *Journal of Physical Chemistry C*, 2009, 113, 10755-10760.

24. L. Li, C. K. Tsung, Z. Yang, G. D. Stucky, L. D. Sun, J. F. Wang, C. H. Yan, *Advanced Materials*, 2008, 20, 903-908.

25. D. R. Baker, P. V. Kamat, *Advanced Functional Materials*, 2009, 19, 805-811.

26. A. I. Hochbaum, D. Gargas, Y. J. Hwang, P. D. Yang, *Nano Letters*, 2009, 9, 3550-3554.

27. Y. Q. Qu, L. Liao, Y. J. Li, H. Zhang, Y. Huang, X. F. Duan, *Nano Letters*, 2009, 9, 4539-4543.

28. Z. H. Kang, C. H. A. Tsang, N. B. Wong, Z. D. Zhang, S. T. Lee, *Journal of the American Chemical Society*, 2007, 129, 12090-12091.

29. C. K. Tsung, J. N. Kuhn, W. Y. Huang, C. Aliaga, L. I. Hung, G. A. Somorjai, P. D. Yang, *Journal of the American Chemical Society*, 2009, 131, 5816-5822.

30. I. K. Konstantinou, T. A. Albanis, *Applied Catalysis B-Environmental*, 2004, 49, 1-14.

31 Y. Ao, J. Xu, D. Fu, X. Shen, C. Yuan, *Colloids and Surface A: Physicochem. Eng. Aspects*, 2008, 312, 125-130.

32. D. Reyes-Coronado, G. Rodríguez-Gattorno, M. E. Espinosa-Pesqueira, C. Cab, R. de Coss, G. Oskam, *Nanotechnology*, 2008, 19, 145605.

33. K. Bücher, J. Bruns, H. G. Wagemann, *Journal of Applied Physics*, 1994, 75, 1127-1132.

34. M. Luhmer, J. B. dEspinose, H. Hommel, A. P. Legrand, *Magnetic Resonance Imaging*, 1996, 14, 911-913.

35. A. P. Legrand, H. Taibi, H. Hommel, P. Tougne, S. Leonardelli, *Journal of Non-Crystalline Solids*, 1993, 155, 122-130.

36. J. P. O'Reilly, C. P. Butts, I. A. I'Anson, A. M. Shaw, *Journal of the American Chemical Society*, 2005, 127, 1632-1633.

37. C. Y. Wang, C. Y. Liu, X. Zheng, J. Chen, T. Shen, *Colloids and Surfaces a-Physicochemical and Engineering Aspects*, 1998, 131, 271-280.

Chapter 3 Hybrid Reduced Graphene Oxide/Silicon Nanowires Structure with Enhanced Photoactivity and Superior Stability

3.1 Introduction

The main hurdle for silicon photocatalyst is the notorious photostability under light illumination due to the surface passivation induced by self-oxidation during photocatalytic process. It is challenging but important to develop effective approaches to stabilize the silicon photoactivity. One important approach to overcome these problems is to develop an inert thin surface protection layer to avoid surface self-oxidation.[1-3] For example, Chen et al. reported to use atomic layer deposition method to deposit a thin TiO_2 protection layers (~2 nm) on the surface of silicon, and the surface protected silicon photoelectrodes exhibited an excellent photostabiltiy for water splitting.[2] However, this method has two-fold drawbacks. The first one is the high costuming atomic layer deposition and this method cannot scale up for large quantities of power photocatalyst; the other problem is the unmatched band structure between silicon and surface coating layer, resulting in the sacrifice of some photoactivity of bare silicon to some extent. Therefore, it is favorable to develop other low cost and scale-up strategies to stabilize the photoactivity of silicon without sacrificing the photoactivity of pristine silicon.

Graphene, a 2D carbon honeycomb lattice structure, has become the hotspot since its discovery, for both fundamental interests and its potential applications in broad areas.[4-8] As for graphene, it has exceptional thermal and chemical stability due to its large scale delocalized carbon-carbon sp^2 bonding. Also, the surfaces of sp carbon allotropes form a natural diffusion barrier thus providing a physical separation.[9] For these reasons, graphene has been used as a passivation layer to protect metal surfaces from oxidation.[9] More importantly, the conducting

graphene carbon sheets can also facilitate charge separation and transportation in semiconductors and their interfaces;[10-12] and graphene sheets possess high optical transparency in visible wavelengths,[13] which will not affect the light absorption of silicon. Therefore, these combined unique properties could make graphene an excellent candidate as a novel protection material for silicon.

Here, we report a facile and simple solution phase method to enwrap silicon nanowires (SiNWs) with reduced graphene oxide sheets (rGO) and the prepared reduced graphene oxide-silicon hybrid structures (rGO-SiNWs) show both enhanced photoactivity and remarkable photostability. The improved photoactivity and photostabilty is mainly attributed to the surface protection of the rGO and more efficient charge separation induced by the formed Schottky junctions at the SiNWs/rGO interface.

3.2 Results and Discussion

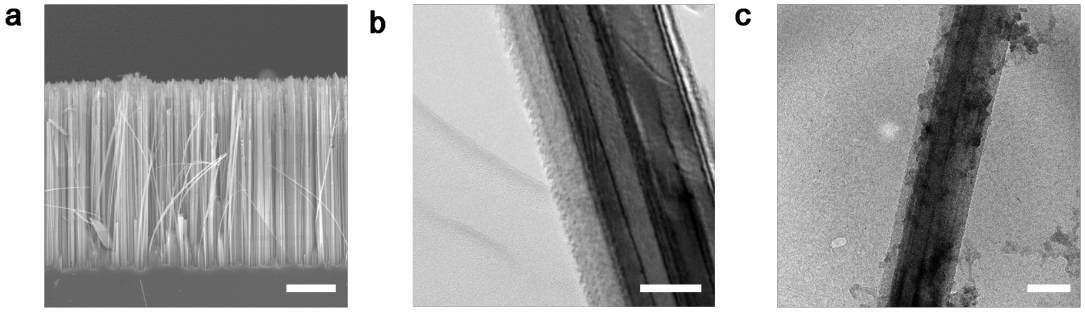

Figure 3.1 (a) Cross sectional SEM image of *p*-type SiNWs. The scar bar is 5 μm. (b) TEM image of bare SiNWs, the scale bar is 50 nm. (c) TEM image of SiNWs functionalized with rGO sheets. The scar bar is 100 nm.

The *p* type SiNWs were prepared by electroless chemical etching with Ag as catalyst. Scanning electron microscopy (SEM) was used to study the surface morphology of the etching

silicon wafer. Figure 3.1a shows the cross sectional SEM image of the etched silicon wafer. It can be seen clearly that SiNWs with a length of around 20 μm have been etched and these nanowires are almost perpendicular to the substrate. These SiNWs grown on silicon wafer can be removed from substrate with a razor blade and collected for further characterization, functionalization and photocatalytic test. We further employed transmission electron microscopy (TEM) to study more detailed surface structure of SiNWs. Figure 3.1b show that the prepared SiNWs has a diameter of around 200 nm. rGO with small size was prepared by modified Hummer's method.[14] In order to make the negatively charged rGO enwrap on the SiNWs, the surface of SiNWs was firstly functionalized with 3-Aminopropyl)triethoxysilane (APTES). Then negatively charged rGO and the positively charged SiNWs were coupled through electrostatic interaction. Figure 3.1c displays the TEM image of SiNWs functioned with small rGO sheets. It clearly shows that numerous small pieces of rGO sheets are closely wrapped on the surface of SiNWs, indicating a physical diffusion barrier between the silicon surface and the ambient environment.

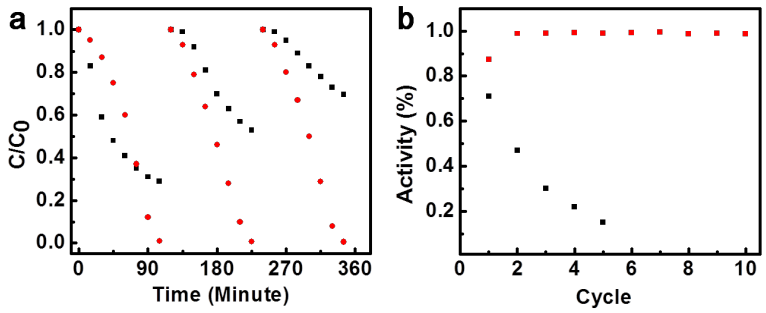

Figure 3.2 (a) The comparison of the IC degradation catalyzed by the SiNWs (black square) and G-SiNWs (red circle) for the first three cycles. (b) The photocatalytic stability of the SiNWs (black square) and G-SiNWs (red circle). The photoactivity of the both photocatalysts is represented by the percentage of IC degraded at the reaction time of 105 minutes for each cycle.

In order to verify our hypothesis that rGO could improve and stabilize the photoactivity of SiNWs, we carried out photocatalytic test on bare SiNWs and rGO-SiNWs, with Indigo carmine (IC) degradation as a case study. The IC degradation was monitored by a Beckman Du-800 UV-vis spectrophotometer as a function of time, to evaluate the photocatalyitc performance of SiNWs and rGO-SiNWs. Figure 3.2a displays the first three photocatalytic cycles of bare SiNWs and rGO-SiNWs. The bare SiNWs shows fast degradation behavior in the first 45 minutes in the first cycle; however, the degradation rate substantially slows down after the first 45 minutes. With the increase of test cycles, the photocatalyitc performance is continuously decreased shown in Figure 3.2a, suggesting the decreased photoactivity is not recoverable in new testing cycles and thus bare SiNWs is not a stable photocatalyst. On the other hand, the rGO enwrapped SiNWs structure shows a superior photoactivity and photostability towards IC dye degradation, with an activation process at the beginning. We later performed photocatalytic cycling studies and compared the photostability of bare SiNWs and rGO-SiNWs, as shown in Figure 3.2b. It clearly displays that the rGO-SiNWs exhibit significantly improved photostability, compared to bare SiNWs. For bare SiNWs, only less than 20% of initial photoactivity is maintained after 5 cycles; as a comparison, rGO-SiNWs do not show any obvious decay in photocatalytic, even after 10 cycles, indicating rGO functionalization is an effective method to improve and stabilize the photoactivity of SiNWs.

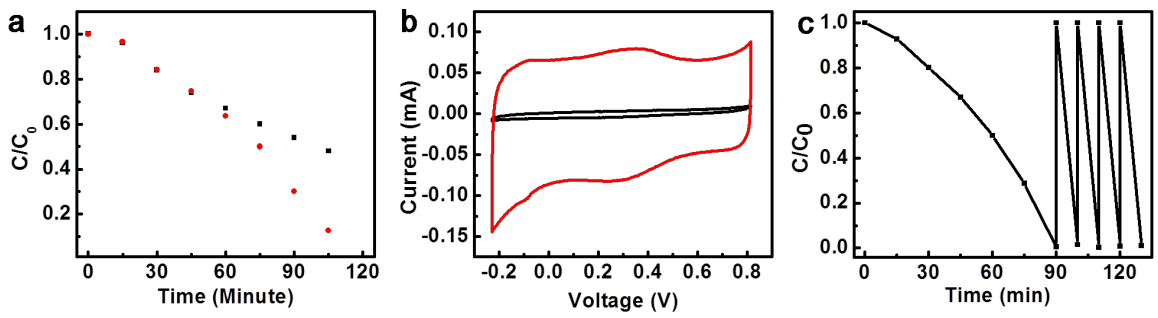

Figure 3.3 (a). IC degradation catalyzed by functionalized rGO-SiNWs (red circle), mechanical mixture of rGO-SiNWs (black square). (b) Cyclic voltammogram curves of bare Si NWs and rGO-SiNWs in 0.5M Na_2SO_4 aqueous solution at a scan rate of 100 mV/s. (c) Continuous IC degradation catalyzed by the SiNWs functionalized with rGO. Calculated amount of IC solution was added after each 10 minutes after a total reaction time of 90 minutes.

Understanding the activation process may help us study the effect of rGO on the improvement of silicon photoactivity and photostability. Therefore, we made the control experiment to prepare mechanical mixture of rGO-SiNWs and study its photocatalytical property. Figure 3.3a shows that the functionalized rGO-SiNWs and mechanical mixed rGO-SiNWs with the same SiNWs/rGO ratio exhibit very similar activation process and photoactivity at the beginning; however, the IC dye degradation rate of mechanically mixed rGO-SiNWs slows down after the activation process, which is different from the functionalized rGO-SiNWs that without any degradation rate decay but similar to the bare SiNWs. This may be attributed to the weak interaction between rGO and SiNWs without functionalization and the detachment readily occurs under strong stirring condition during the photocatalytic process. Importantly, both mechanical mixed and functionalized rGO-SiNWs shows activation process, indicating rGO is the key factor for the activation process. Considering the large surface area of rGO, we hypothesize the activation process is probably due to the light driven internal charging effect. Under light irradiation, the electron-hole pairs are generated in SiNWs and then separated to charge rGO sheet based electrochemical capacitors on SiNWs. Finally, both the electrons and holes in the fully charged electrochemical capacitors jump into solution and degrade IC dye, respectively. As a result, the activation time in the photocatalytic process can be understood that the photoexcited electron/hole pairs are not used for IC dye degradation, until the rGO based

electrochemical capacitors are fully charged. Figure 3.3b shows the cyclic voltammgrams (CV) of the same amount of bare SiNWs and functionalized G-SiNWs in 0.5M Na_2SO_4 aqueous solution with a scan rate of 100 mV/s. it clearly shows that rectangular CV area has been significantly increase after rGO functionalization, indicating the charge storage capability of rGO-SiNWs is substantially larger than bare SiNWs. This explains why the photocatalytic process exhibits activation time with rGO modification. If this mechanism is true, the activation time is not needed with continuous dye addition at the end of each cycle. We further performed the cycling control experiment by adding calculated IC dye into the reaction system, without centrifuging out the photocatalyst. The cycling curve of IC dye degradation is shown in Figure 3.3c. As expected, the photocatalytic activity is significantly increased without activation time, compared to the first IC dye degradation cycle. The enhanced IC dye degradation rate after first cycle is attributed to the already fully charged electrochemical capacitor on SiNWs and self-activation process is not needed anymore. All these results have demonstrated the rGO is the key factor for the activation process in the photocatalytic reaction and efficient IC dye degradation occurs after the rGO sheets on SiNWs are fully charged.

In order to probe the impact of rGO on the charge separation at the interface between SiNWs and rGO and understand how rGO enhances the photoactivity of SiNWs, we further conducted electrochemical and photoelectrochemical studies on both bare SiNWs and rGO-SiNWs. Considering one of the photocatalytic reactions involves oxygen reduction to generate reactive oxygen species (ROS), we studied the sensitivity of rGO to oxygen reduction. Figure 3.4a shows the cyclic voltammograms of same amount of bare SiNWs and rGO-SiNWs in 0.5M Na_2SO_4 solution with/without oxygen. It clearly shows that rGO-SiNWs exhibit obvious oxygen reduction property, compared to bare SiNWs. This result indicates rGO could facilitate

oxygen reduction during the photocatalytic process and thus improve the photoactivity of the SiNWs.

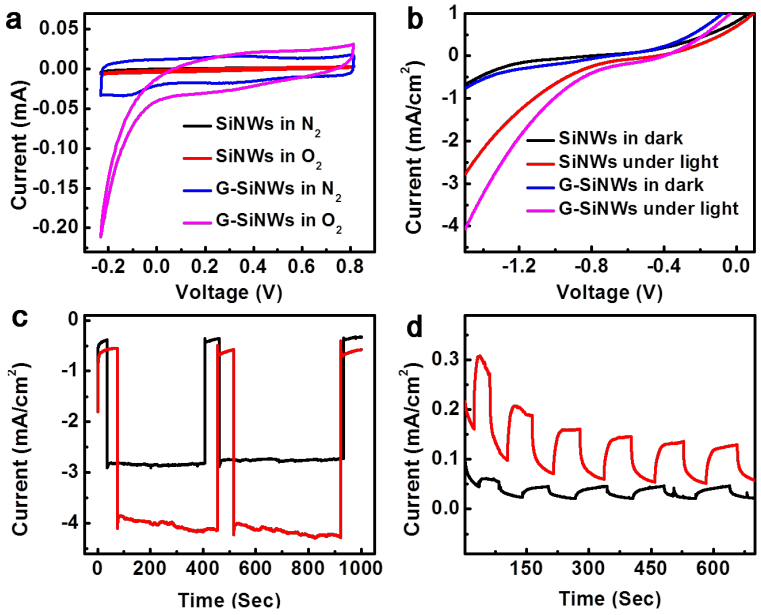

Figure 3.4. (a) Cyclic voltammograms of bare SiNWs and G-SiNWs in 0.5 M Na_2SO_4 aqueous solution under N_2 and O_2 condition. (b) Linear sweep of SiNWs and G-SiNWs in 0.5M Na_2SO_4 aqueous solution with IC dye under dark condition and light illumination. (c) Photocurrent response of bare SiNWs (black curve) and G-SiNWs (red curve) at the potential of -1.5V vs. Ag/AgCl under chopped light illumination. (d) Photocurrent response of bare SiNWs (black curve) and G-SiNWs (red curve) with fixed potential of 1V vs. Ag/AgCl under chopped light illumination.

By photoelectrochemical method, we further study the photoexcited charge separation at the interface between rGO and SiNWs. Figure 3.4b shows the linear sweep of bare SiNWs and rGO-SiNWs in 0.5M Na_2SO_4 solution with IC dye at the scan rate of 50 mV/s, under dark condition and light illumination. As expected, both SiNWs and rGO-SiNWs show cathodic photocurrents and the rGO modification could enhance the photocurrent of SiNWs in the negative potential region. The increased photocurrent is believed to attribute to the more efficient

electron injection from silicon to rGO (Figure 3.4c). On the other hand, in order to study the hole separation in silicon/rGO interface, we applied a reversible (positive) bias on silicon photoelectrodes to tune the *p*-type property to n type behavior. As we can see in Figure 3.4d, both bare SiNWs and rGO-SiNWs show anodic photocurrent response with applying a positive potential of 1.0V vs. Ag/AgCl. Interestingly, the rGO-SiNWs sample also owns higher photocurrent density than that of bare SiNWs, suggesting rGO can also facilitate hole transport at the rGO/Si interface. It is believed that different degree of reduction of the rGO would form different Schottky junctions with SiNWs. With a high degree of reduction, parts of rGO would have a Fermi level around 4.5ev more like graphene.[15] These parts of rGO in junction with silicon would serve as the electron transporter. While with a low degree of reduction, parts of rGO would have a Fermi level around 4.9ev more like graphene oxide.[16,17] And these parts of rGO in junction with silicon would serve as the hole transporter. Therefore, the enhanced photoexcited charges separation for both holes and electrons in SiNWs could not only prevent the self-oxidation of the silicon, but also improve the photoactivity of silicon.

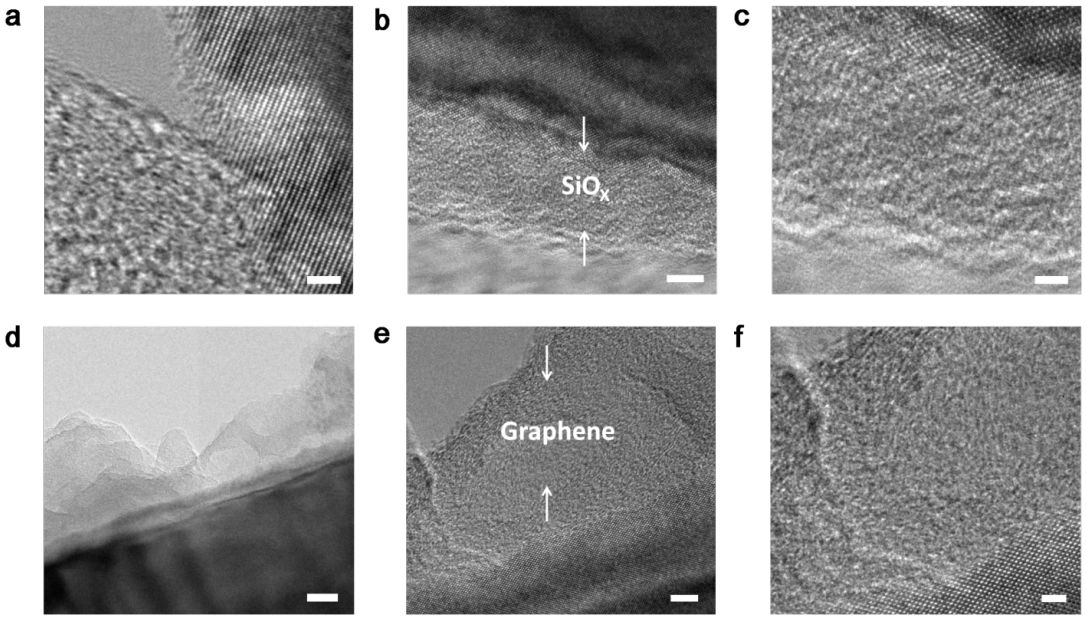

Figure 3.5 (a) HRTEM image of as prepared bare SiNWs before photocatalytic testing. (b,c) HRTEM images of bare SiNWs after photocataltyic reaction. The arrow indicates the formed silicon dioxide shell. The scar bars are 5 nm and 2 nm. (d-f) TEM and HRTEM images of SiNWs functionalized with rGO after reaction. The arrow indicates the rGO shell on SiNWs surface. The scar bars are 20 nm and 5 nm and 2 nm.

We further conducted TEM studies on bare SiNWs and rGO-SiNWs after photocatalytic testing, to verify our conclusion that rGO modification could avoid the self-oxidation of SiNWs. Figure 3.5a shows the TEM image of as prepared bare SiNWs before photocatalytic testing. The clean and smooth surface indicates silicon oxide is absent at the surface of freshly prepared SiNWs. After photocatalytic testing, the surface of bare SiNWshas been covered by a 5-10 nm amorphous SiO_2 shell shown in Figure 3.5b and 3.5c, suggesting the SiNWs has been oxidized during photocatalytic process. As a comparison, Figure 3.5d-f show that silicon nanowires are well protected by the enwrapping rGO sheets and the silicon surface is in good contact with rGO without any SiO_2 shell, indicating that the rGO modification is an effective method to prevent SiNWs from self-oxidation.

3.3 Conclusions

In summary, we have firstly developed a novel, low cost and effective strategy to protect SiNWs from oxidation by functionalizing with thin layer rGO sheets and used them as highly efficient and stable photocatalyst for dye degradation. Photocatalytic testing shows that the rGO enwrapped SiNWs showed superior stability and photoactivity, compared to the unprotected SiNWs and the activation process at the beginning of the photocatalytic reaction is attributed to photo-charging effect induced by graphene sheets. Electrochemical and photoelectrochemical studies demonstrate that the enhanced photoactivity and photostabilty is due to the more efficient

photo-excited charge separation on SiNWs, and thus it can avoid the self-oxidation on silicon surface during photocatalytic dye degradation. The prepared stable and efficient rGO enwrapped silicon nanowire photocatalyst could have enormous impact on the design and application silicon based materials for visible-light photocatalytic organic waste treatment and environmental remediation.

3.4 Materials and Method

Material Preparation. The SiNWs in this study were synthesized on *p* type silicon wafer (10-30 Ω·cm) through a wet chemical etching method. Briefly, the silicon pieces were sonicated in acetone and isopropyl alcohol first and then immersed into a buffered oxide etchant (BOE) to remove the native oxide layer. The H-terminated silicon pieces were coated with Ag by solution electroless deposition in a solution containing 0.005M AgNO3 and 4.8 M HF for 1 min at room temperature. After Ag deposition, the color of the silicon wafer surface turn from dark to colorful. the obtained silver coated silicon wafer was further rinsed with de-ionized water to remove extra silver ions and then immediately immersed into an etching solution containing 4.8M HF and 0.3M H_2O_2 for 40 minutes. Finally, the Ag nanoparticles was removed from the nanowires by immersing in concentrated nitric acid for one hour. The SiNWs were then scratched down by a razor blade and collected for further functionalization. Graphene oxide sheets were prepared through Hummers' method and followed by strong sonication. The as-prepared graphene oxide was further reduced by hydrazine solution and the reduced graphene oxide solution was directly used for the subsequent studies without further purification. 1 mg of SiNWs powder were dispersed in 3 ml of 2% (3-Aminopropyl)triethoxysilane (APTES) ethanol solution, stirred for 2 h and then centrifuged and washed out with ethanol for three times. The APTES functionized SiNWs were re-dispersed in 5 ml of water and mixed with various amount (1-4 mg) of rGO for 2

h under vigorous stirring. The product was finally centrifuged and washed with water for three times.

Material Characterization. The SiNWs were study with a scanning electron microscope (SEM) (JEOL 6700) at 10 kV of electron acceleration voltage. Transmission electron microscopy (TEM) and high resolution TEM (HRTEM) imaging of the SiNWs and the rGO wrapped SiNWs was conducted on Phillips CM120 with a 120 kV operation voltage and FEI Titan with a 300 kV operation voltage, respectively.

Photocatalytic test. Photocatalytic degradation reaction was studied with SiNWs or G-SiNWs in 100 mM of Indigo carmine (IC) aqueous solution under a 300 W xenon lamp. The IC degradation was monitored by a Beckman DU-800 UV-vis spectrophotometer. All photocatalytic reactions were carried out under ambient conditions. Raman study was performed by a Raman spectroscopy (Renishaw 1000, 514 nm laser wavelength, 50 × objective). Electrochemical and photoelectrochemical studies were carried out on Princeton Applied Research electrochemical workstation coupled with a xeon lamp.

3.5 Bibliography

1. M. J. Kenney, M. Gong, Y. G. Li, J. Z. Wu, J. Feng, M. Lanza, H. J. Dai, *Science* 2013, 342, 836-840.

2. Y. W. Chen, J. D. Prange, S. Duhnen, Y. Park, M. Gunji, C. E. D. Chidsey, P. C. McIntyre, *Nat. Mater.* 2011, 10, 539-544.

3. K. Jun, Y. S. Lee, T. Buonassisi, J. M. Jacobson, *Angew. Chem.-Int. Edit.* 2012, 51, 423-427.

4. J. W. Bai, X. Zhong, S. Jiang, Y. Huang, X. F. Duan, *Nat. Nanotechnol.* 2012, 5, 190-194.

5. L. Liao, J. W. Bai, R. Cheng, Y. C. Lin, S. Jiang, Y. Huang, X. F. Duan, *Nano Lett.* 2010, 10, 1917-1921.

6. J. W. Bai, R. Cheng, F. X. Xiu, L. Liao, M. S. Wang, A. Shailos, K. L. Wang, Y. Huang, X. F. Duan, *Nat. Nanotechnol.* 2010, 5, 655-659.

7. L. Liao, Y. C. Lin, M. Q. Bao, R. Cheng, J. W. Bai, Y. A. Liu, Y. Q. Qu, K. L. Wang, Y. Huang, X. F. Duan, *Nature* 2010, 467, 305-308.

8. Y. Liu, R. Cheng, L. Liao, H. L. Zhou, J. W. Zhou, G. Liu, L. X. Liu, Y. Huang, X. F. Duan, *Nat. Commun.* 2011, 2, 7.

9. S. S. Chen, L. Brown, M. Levendorf, W. W. Cai, S. Y. Ju, J. Edgeworth, X. S. Li, C. W. Magnuson, A. Velamakanni, R. D. Piner, J. Y. Kang, J. Park, R. S. Ruoff, *ACS Nano* 2011, 5, 1321-1327.

10. Q. J. Xiang, J. G. Yu, M. Jaroniec, *Chem. Soc. Rev.* 2012, 41, 782-796.

11. Q. J. Xiang, J. G. Yu, *J. Phys. Chem. Lett.* 2013, 4, 753-759.

12. H. Y. Wu, M. Xu, P. M. Da, W. J. Li, D. S. Jia, G. F. Zheng, *Phys. Chem. Chem. Phys.* 2013, 15, 16138-16142.

13. S. Bae, H. Kim, Y. Lee, X. F. Xu, J. S. Park, Y. Zheng, J. Balakrishnan, T. Lei, H. R. Kim, Y. I. Song, Y. J. Kim, K. S. Kim, B. Ozyilmaz, J. H. Ahn, B. H. Hong, S. Iijima, *Nat. Nanotechnol.* 2010, 5, 574-578.

14. W. S. Hummers, R. E. Offeman, *J. Am. Chem. Soc.* 1958, 80, 1339-1339.

15. J. Debgupta, S. Mandal, H. Kalita, M. Aslam, A. Patra, V. Pillai, *RSC Adv.* 2014, 4, 13788-13795.

16. E. Stratakis, K. Sawa, D. Konios, C. Petridis, E. Kymakis, *Nanoscale* 2014, DOI: 10.1039/C4NR01539H.

17. A. B. Yusoff, H. P. Kim, J. Jang, *Sol. Energy Mater. Sol. Cells* 2013, 109, 63-69.

Chapter 4 High Capacity Silicon-Air Battery in Alkaline Solution

4.1 Introduction

The ever increasing demand for portable power source has motivated considerable research efforts in various power/energy systems.[1-9] With the reduction of oxygen from the environment as its cathodic reaction, metal-air battery is known for its high energy density.[10] As the first commercialized metal-air battery, zinc-air battery has garnered significant attention since 1960s,[11-15] and has more recently gained renewed interest for the application in electric vehicles.[16] However, zinc-air battery can only provide a practical energy density of 470 Wh/kg out of a theoretical value of 1370 Wh/kg.[17] Aluminum-air battery has a high theoretical energy density (8100 Wh/kg),[18,19] but is limited to military applications due to its high self discharge rate.[20] Alloying the aluminum with tin or other proprietary elements has made the battery electrodes less corrosive in the alkaline solution.[21,22] As an alternative to aluminum and zinc, lithium-air battery possesses a higher theoretical energy density of 13000 Wh/kg and an expected practical value of 1700 Wh/kg,[23-25] but it can be compromised by potential safety and cost issues.[26-28] Silicon-air battery can be another interesting system with a theoretical energy density of 8470 Wh/kg, which is less than lithium-air systems but compares favorably to the zinc- or aluminum-air system. Additionally, unlike lithium, silicon is one of the most abundant elements on the earth, and therefore may offer a cost-effective alternative. Most recently, a silicon-air battery was reported using EMI·(HF)2.3F ionic liquid based electrolyte.[29,30] This battery system showed an unlimited shelf-life with a working potential in the range of 1.0-1.2 V. The practical application of this battery system, however, can be complicated due to severe chemical safety issues associated with the fluoride based electrolyte.

Herein we report a high capacity silicon-air battery using nanostructured silicon and alkaline solution based electrolyte that only involves environmentally friendly elements such as silicon, potassium, oxygen and hydrogen. The silicon surface is first modified by the metal assisted electroless chemical etching method. [31-35] The assembled battery displays a flat and stable discharge curve with a voltage ranging from 0.9 to 1.2 V (under different discharge current densities) over days. In contrast, the unmodified silicon wafer becomes passivated quickly in the alkaline solution and therefore the potential drops rapidly after discharging for a short period of time (minutes). We propose that the formation of the porous surface structure increases the overall $Si(OH)_4$ dissolving rate in the KOH electrolyte, which effectively removes the oxide and reactivates the silicon surface. The corrosion of the silicon in the KOH electrolyte is also carefully investigated to minimize the self-discharge. It is found that the corrosion of the silicon can be effectively minimized with a lower KOH concentration (0.6 M), enabling a specific capacity as high as 1206.0 mA·h/g, which is about 2 times of the practical value of commercial zinc-air battery (~650 mA·h/g, Energizer) [36] and 3 times higher than that of the commercial aluminum-air battery (~320 mA·h/g, Altek Fuel Group Inc.). [37]

4.2 Results and Discussion

Figures 4.1a and 4.1b show a schematic illustration of a silicon-air battery device and a photograph of a real one. We have employed a simple device architecture consisting of a surface modified silicon wafer as the anode, an air diffusion electrode as the cathode, a polydimethylsiloxane (PDMS) stamp with an open-through hole sandwiched between the silicon wafer and air diffusion electrode as the cell, and variable concentrations of potassium hydroxide solution as the electrolyte.

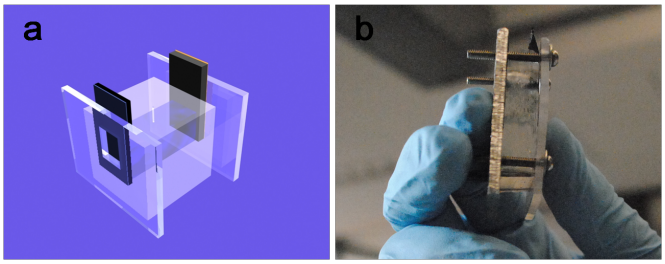

Figure 4.1 (a) A schematic illustration of alkaline based silicon-air battery. (b) A real picture of a silicon-air battery.

Figures 4.2a and 4.2b show the scanning electron microscopy (SEM) images of the top view and cross-sectional view of a silicon wafer after the metal-assisted electroless etching process. This process creates a ~1.5 μm micro-porous layer of silicon nanowire bundles on top of the silicon surface, and therefore significantly roughs the substrate surface. The roughed silicon substrate is then used as the anode in the air-battery system. Typical galvanostatic discharge characteristics of the device show that it can be continuously discharged before the silicon source is used up (only shows data for 30 hours here) with an operating potential of 1.2 V (with discharge current density of 0.05 mA/cm^2) (Figure 4.2c). In contrast, in a control experiment with unmodified silicon wafer, the device can only be discharged for less than 10 minutes at a lower potential of 1.1 V before the potential quickly drops to zero (Figure 4.2d). These studies clearly demonstrate that the rough surface is a critical factor responsible for the sustained discharging.

The discharge process can be described as electrochemical reactions of the anode and cathode. [38,39]

At the anode,

$$Si + 4OH^- \rightarrow Si(OH)_4 + 4e^- \quad (E_0=1.69\ V) \qquad (1)$$

At the cathode,

$$O_2 + 2H_2O + 4e^- \rightarrow 4OH^- \quad (E_0 = 0.40\ V) \qquad (2)$$

The anode oxidation product $Si(OH)_4$ needs to be promptly removed from the electrode surface to ensure continuous discharge. The presence of alkaline ensures that the $Si(OH)_4$ can be dissolved and keeps the silicon surface free of oxide. However, when the dissolving rate of the $Si(OH)_4$ in KOH is slower than the production rate, $Si(OH)_4$ can build up on the silicon surface, leading to the formation of the SiO_2 to passiviate the surface and prevent the battery from continuous discharging. In our experiment, the oxidation rate is calculated to be 50-100 nm/hour (for a smooth planar wafer) under the discharge current density of 0.05 mA/cm^2 while the SiO_2 dissolving rate is only around 1~2 nm/hour at room temperature.[38,39] Therefore, for the unmodified silicon with flat surface, the silicon oxide formation rate far exceeds its dissolving rate, and the surface is covered by silicon oxide and turns passivated very quickly, resulting in the short lifetime of the battery. On the other hand, through the surface modification, the surface area of the silicon substrate can be considerably increased by orders' magnitude[31] and the electrolyte can easily diffuse into the pores. With this increased surface area, the overall oxide dissolving rate can be increased to surpass the oxide formation rate (passivation rate). As a result, the oxide at the silicon surface can be continuously etched away and the surface keeps refreshed for continued discharge. Figures 4.2e and 4.2f are the SEM images of surface morphologies of modified and unmodified silicon wafer taken immediately after discharge, respectively. As expected, the modified one presents a highly porous surface structure while the unmodified one retains its smooth surface.

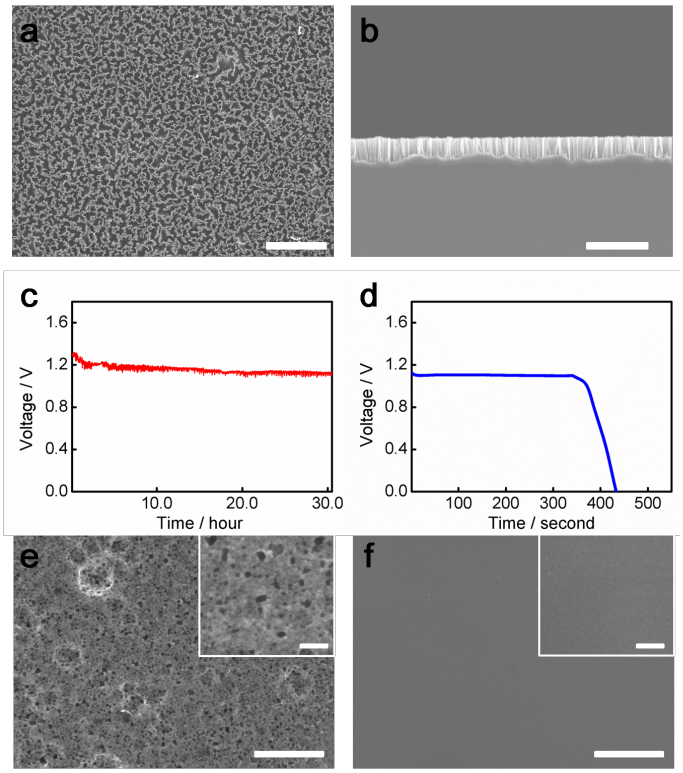

Figure 4.2 (a) Top view SEM image of the silicon wafer after surface modification. (b) Cross-sectional view SEM image of the silicon wafer after surface modification. (c) Galvanostatic discharge curve of modified silicon-air battery. The discharge current density is 0.05 mA/cm^2. (d) Galvanostatic discharge curve of unmodified silicon-air battery. The discharge current density is 0.05 mA/cm^2. (e) Top view SEM image of modified silicon after discharge. (f) Top view SEM image of unmodified silicon after discharge. The main scale bars are 5 μm, and the scale bars in the inset are 1 μm.

To further probe the discharge process, a 5-hour stepped discharge measurement is performed under various discharge current densities (Figure 4.3a, black curve). The current densities are increased stepwise from 0.01 mA/cm^2 to 0.1 mA/cm^2 and then stepped back to 0.01mA/cm^2. It is observed that with increasing discharge current density, the operating potential decreases. This potential drop might be attributed to the internal resistance present between silicon/electrolyte interfaces. We also investigate the impact of the dopant concentration of the

silicon wafer on the cell performance (Figure 4.3a). In general, silicon wafer with higher dopant concentration displays a higher operating voltage, which we believe can be attributed to the lower internal resistivity of the highly doped silicon wafer.

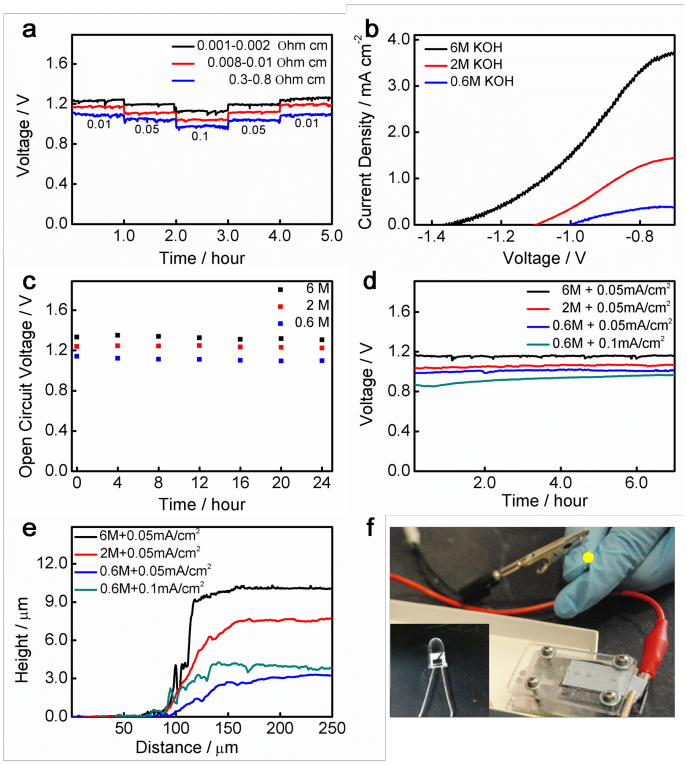

Figure 4.3 (a) Galvanostatic discharge curve of modified silicon-air battery with various dopant concentrations and discharge current densities (mA/cm^2). (b) Linear sweep voltammograms of modified silicon wafer as electrode in KOH solutions with various concentrations as the electrolyte. (c) Open circuit voltage plots measured for 24 hours with various KOH concentrations. (d) Galvanostatic discharge curve of modified silicon-air battery in KOH solutions with various concentrations and discharge current densities. (e) Step heights between the reacting and non-reacting area of the modified silicon in KOH solutions with various concentrations and discharge current densities. f) Lighting a LED with silicon-air batteries.

The self-discharge is usually a serious issue in the alkaline solution based metal-air system,

particularly for the aluminum-air battery.[20] Similarly, it is also a critical challenge in silicon-air battery system. Since the self-discharge rate is highly dependent on the electrolyte composition, we have investigated the KOH concentration effect on the silicon-air battery. Figure 4.3b is the polarization curve of surface modified silicon in various KOH concentrations. As expected, with higher KOH concentration, the anodic dissolution potential is higher (more negative). Generally, a more negative anodic dissolution potential is favorable for higher open circuit voltage (OCV) or operating voltage. The OCV measurements with various KOH concentrations in Figure 4.3c are consistent with polarization curves. The values at 6 M, 2 M, 0.6 M KOH are 1.32 ± 0.01 V, 1.23 ± 0.01 V and 1.10 ± 0.01 V for 24 hour measurements. It is found that the OCV of the cell at high KOH concentration (6 M) is still much lower than the theoretical value of 2.09 V. This phenomenon has also been observed in aluminum-air battery system, which can be partially attributed activation polarization (over-potential) and the partial formation of an anodic passivation layer.[17] The discharge plots with various KOH concentrations in Figure 4.3d are also consistent with polarization curves. With increasing KOH electrolyte concentration (0.6 M, 2 M, 6 M), the operating potentials are 1.01 V, 1.06 V and 1.18 V at a discharge current density of 0.05 mA/cm^2, respectively. However, the tradeoff for the high operating potential brought by the high KOH concentration is the high silicon corrosion (self-discharge) rate. The overall chemical corrosion reaction by alkaline is given by[38,39]

$$Si + OH^- + 2H_2O \rightarrow SiO_2(OH)_2^{2-} + 2H_2 \qquad (3)$$

Here silicon reacts with hydroxide ions and produces $SiO_2(OH)_2^{2-}$ and hydrogen gas bubbles. To quantify the corrosion effect of KOH in our device, batteries are filled with KOH with various concentrations and discharged for 7 hours at a current density of 0.05 or 0.1 mA/cm^2 (Figure 4.3d). After the reaction, we measured the step difference between the reacting and non-reacting

area of the silicon (Figure 4.3e). The step heights difference between the reacting and non-reacting region (including 1.5 μm micro-porous layer) are measured to be 11.0 μm, 8.2 μm and 3.3 μm for 6 M, 2 M and 0.6 M KOH electrolyte, respectively. Considering the volume percentage of the micro-porous layer is about 20%, the total amounts of silicon consumed are about 9.8 μm, 7.0 μm and 2.1 μm for 6 M, 2 M and 0.6 M KOH electrolyte. Additionally, we can calculate the silicon consumed by the oxidative discharge to be 0.4 μm based on the discharge current density and time. Therefore, the amounts of silicon consumed by the self corrosion are about 9.4 μm, 6.6 μm and 1.7 μm in the 6 M, 2 M and 0.6 M KOH solution, corresponding to an average corrosion rate of 1.34 μm/h, 0.95 μm/h and 0.24 μm/h, respectively.[38] The estimation suggests that one can in principle expect a respectable lifetime of ~2000 hours for a 500 μm thick silicon wafer with a low KOH concentration.

The specific capacities of the silicon-air battery with various KOH concentrations and discharge current densities are then calculated and summarized in Table 4.1 To make a fair comparison with other anode materials, the weight of the anode silicon consumed is used for the capacitance calculation. The loss of the specific capacity is severely aggravated in the concentrated KOH solution (6 M) as most of the silicon is wasted in the self-discharge process. However, as self-corrosion is substantially reduced by lowering the KOH concentration, the specific capacity increases significantly. With a diluted KOH concentration (0.6 M) and a discharge current density of 0.1 mA/cm^2, the silicon-air battery can reach a specific capacity as high as 1206.0 mA·h/g, which is much higher than the practical values of commercial zinc-air battery (650 mA·h/g, electrical capacity 620 mA·h, cell weight, 1.9 g, zinc anode weight percentage, ~50%, Energizer) and aluminum-air battery (~320 mA·h/g, electrical capacity, 120 A·h, aluminum anode weight, 0.37 kg, Altek Fuel Group Inc.). [36,37] Nonetheless, considering that

the theoretical specific energy density of silicon-air system is 8470 Wh/kg, our device can be further optimized in terms of device configuration and other experimental parameters to reach even higher energy density. We also note the solubility of $Si(OH)_4$ in the electrolyte solution can impact the eventual capacity of the practical silicon-air battery. Additional work is clearly needed to fully understand oxidative discharge and self-corrosion process as well as their dependence on surface structures, anode and electrolyte compositions, and therefore to develop a practical system with optimized discharge current density and minimum self-corrosion.

The formation of the silicon-air battery can be readily used to drive practical devices. To demonstrate this point, two silicon-air batteries are assembled in serial connection for battery testing. The serially connected silicon-air batteries can be readily used to light up a semiconductor light-emitting diode (LED) (2.1 volts required) (Figure 4.3f).

Discharge current density (mA/cm^2)	KOH concentration (M)	Weight of silicon (mg)	Specific capacity (mA·h/g)
0.05	6	2.26	154.8
0.05	2	1.63	214.7
0.05	0.6	0.49	715.7
0.1	0.6	0.58	1206.0

Table 4.1 Specific capacities of silicon-air battery with various KOH concentrations and discharge current densities.

4.3 Conclusions

In conclusion, we have successfully fabricated a new alkaline solution based silicon-air battery and demonstrated its potential as a high capacity power source. The sustainable discharge

profile in the alkaline solution can be attributed to the surface modification of the starting silicon wafer, which substantially enlarges the surface contacting area between the silicon and electrolyte and the subsequent $Si(OH)_4$ dissolving rate. The assembled battery can provide an operating potential ranging from 0.9 to 1.2 V, with various current densities of 0.01 to 0.1 mA/cm^2. The self-corrosion of the silicon by the alkaline solution can be effectively reduced by lowering the concentration of the electrolyte to some extent, however, with a partial sacrifice of the output potential. Specific capacity as high as 1206.0 mA·h/g is achieved, which is substantially larger than the practical value of the commercialized zinc-air battery (~650 mA·h/g)[36] and that of the commercial aluminum-air battery (~320 mA·h/g).[37] Further improvements in the configuration of the cell, material surface roughness, electrolyte concentration, wafer dopant type and concentration, air diffusion electrode are expected to allow the design of eco-friendly silicon-air battery with higher capacity and energy density. Importantly, unlike many other battery systems, the alkaline solution based silicon-air battery system described here only involves common elements such as silicon, potassium, oxygen and hydrogen, and therefore may offer an environmentally friendly solution for future mobile power requirements. In combination with the established fields of silicon industry, this alkaline based silicon-air battery may lead to a new class of power embedded system, opening up a new generation of self-powered silicon based device applications such as Micro-Electro-Mechanical Systems (MEMS), integrated circuit (IC) and electrical vehicles (EVs).

4.4 Materials and Method

Material preparation. The silicon wafers investigated in this study were n-type, with the resistivity of 0.001-0.002 Ω·cm. The clean silicon pieces were immersed into a buffered oxide etchant (BOE) to remove the native oxide layer. The Hydrogen-terminated silicon pieces were

coated with Ag by the solution electroless deposition method described in our previous work.[31] Following the Ag deposition, the silicon pieces were placed into an etching solution containing 4.8 M HF and 0.3 M H_2O_2 for 2 minutes. After the reaction, the samples were thoroughly washed with a large amount of water. The Ag nanoparticles were removed by soaking the samples into concentrated nitric acid for approximately one hour. Finally, the silicon pieces were rinsed with water several times and dried with nitrogen flow. Gold thin film with a titanium adhesion layer is evaporated on the backside of the silicon wafer as contact.

Battery cell. The battery device consisting of a surface modified silicon wafer (~1.5 cm × 2 cm, 500 mm thick), an air diffusion electrode (Purchased from Quantumsphere Co. Ltd) and a polydimethylsiloxane (PDMS) stamp with an open-through hole (~0.5 cm diameter) was sandwiched tightly by aluminum sheet and plastic plate with open windows at the center of the air electrode to allow air diffusion. Potassium hydroxide with various concentrations (0.6 M, 2 M, 6 M) were injected into the cell as the electrolyte.

Electrochemical test. Galvanostatic and linear sweep voltammograms were performed on VersaSTAT 4 from Princeton Applied Research. Open circuit voltage (OCV) was measured by storing the cell in an open-circuit condition for 24 hours at room temperature. Step height data was collected by a Dektak 8 profilometer.

4.5 Bibliography

1. C. A. Vincent, B. Sccrosati, in *Modern Battery,* Elsevier, 1997, pp. 98-103.

2. S. Xu, Y. Qin, Y. G. Wei, R. S. Yang, Z. L. Wang, *Nature* 2010, 5, 366-373.

3. G. Zhu, R. S. Yang, S. H. Wang, Z. L. Wang, *Nano Lett.* 2010, 10, 3151-3155.

4. X. Zhao, T. Wu, S. T. Zheng, L. Wang, X. H. Bu, P. Y. Feng, *Chem. Commun.* 2011, 47, 5536-5538.

5. W. W. Zhou, C. W. Cheng, J. P. Liu, Y. Y. Tay, J. Jiang, X. T. Jia, J. X. Zhang, H. Gong, H. H. Hng, T. Yu, H. J. Fan, *Adv. Funt. Mater*. 2011, 21, 2439-2445.

6. J. P. Liu, C. W. Cheng, W. W. Zhou, H. X. Li, H. J. Fan, *Chem. Commun*. 2011, 47, 3436-3438.

7. H. L. Wang, H. S Casalongue, Y. Y. Liang, H. J. Dai, *J. Am. Chem. Soc.* 2010, 132, 15920-15923.

8. H. L. Wang, L. F. Cui, Y. Yang, H. S. Casalongue, J. T. Robinson, Y. Y. Liang, Y. Cui, H. J. Dai, *J. Am. Chem. Soc.* 2010, 132, 13978-13980.

9. X. M. Sun, J. F. Liu, Y. D. Li, *Chem. Mater.* 2006, 18, 3486-3494.

10. V. Neburchilov, H. J. Wang, J. J. Martin, W. Qu, *J. Power Sources* 2010, 195, 1271-1291.

11. K. F. Blurton, A. F. Sammells, *J. Power Sources* 1979, 4, 263.

12. C. Chakkaravarthy, H. V. K. Udupa, *J. Power Sources* 1983, 10, 197.

13. F. Charmran, H. S. Min, B. Dunn, C. J. Kim, *20th IEEE International Conference on Micro Electro Mechanical Systems - MEMS* 2007, 871-874.

14. T. Wang, M. Kaempgen, P. Nopphawan, G. Wee, S. Mhaisalkar, M. Srinivasan, *J. Power Sources* 2010, 195, 4350-4355.

15. L. Fu, J. K. Luo, J.E. Huber, T. J. Lu, *J. Physics: Conference Series* 2006, 34, 800-805.

16. J. Goldstein, B. Koretz, *IEEE Aerospace Electron. Syst. Mag.* 1993, 8, 36.

17. C. J. Lan, T. S. Chin, P. H. Lin, T. P. Perng, *J. New Materials for Electrochemical Systems* 2006, 9, 27-32.

18. Y. Hori, J. Takao, H. Shomon, *Electrochim. Acta* 1985, 30, 1121.

19. C. S. Li, W. Q. Ji, J. Chen, Z. L. Tao, *Chem. Mater.* 2007, 19, 5812-5814.

20. A. A. Mohamad, *Corrosion Science* 2008, 50, 3475-3479.

21. D. Chartouni, N. Kuriyama, T. Kiyobayashi, J. Chen, *J.Alloys and Compounds* 2002, 330-332,766-770.

22. A. A. Mohamada, N. S. Mohamedb, Y. Aliasc, A. K. Arofa, *J. Power Sources* 2003, 115, 161-166.

23. A. Kraytsberg, Y. Ein-Eli, *J. Power Sources* 2011, 196, 886-893.

24. G. Girishkumar, B. McCloskey, A. C. Luntz, S. Swanson, and W. Wilcke, *J. Phys. Chem. Lett.* 2010,1,2193-2203.

25. J. S. Lee, S. T. Kim, R. G. Cao, N. S. Choi, M. Liu, K. T. Lee, J. Cho *Adv. Energy Mater.* 2011, 1, 34–50

26. E. L. Littauer, K. C. Tsai, *J. Electrochem. Soc.* 1977, 124, 850.

27. K. M. Abraham, Z. Jiang, *J. Electrochem. Soc.* 1996, 143, 1.

28. M. Armand and J. M. Tarascon, *Nature* 2008, 451, 652-657.

29. G. Cohn, Y. Ein-Eli, *J. Power Sources* 2010, 195, 4963-4970.

30. G. Cohn, D, Starosvetsky, R. Hagiwara, D. D. Macdonald, Y. Ein-Eli, *Electrochemistry Communications* 2009, 11, 1916-1918.

.31.X. Zhong, Y. Q. Qu, Y. C. Lin, L. Liao, X. F. Duan, *ACS Applied Materials&Interface* 2011, 3, 261–270.

32. Y. Q. Qu, L. Liao, Y. J. Li, H. Zhang, Y. Huang, X. F. Duan, *Nano Lett.* 2009, 9, 4539–4543.

33. Y. Q. Qu, X. Zhong, Y. J. Li, L. Liao, Y. Huang, X. F. Duan, *J. Mater. Chem.* 2010, 20, 3590–3594.

34. Y. Q. Qu, X. Zhong, X. F. Duan, *Advanced Functional Material* 2010, 20, 3005-3011.

35. M. Xue, X. Zhong, Z. Shaposhnik, Y. Q. Qu, F. Tamanoi, X. F. Duan, J. I. Zink, *J. Am. Chem. Soc.* 2011, 133, 8798-8801.
36. http://data.energizer.com/PDFs/675.pdf.
37. http://altekfuel.com/userfiles/File/SDS_APS100_12-24_V-04.pdf.
38. X. G. Zhang, in *Electrochemistry of silicon and its oxide,* Springer, 2001, pp. 294-297.
39. M. J. Madou, in *Fundamentals of microfabrication,* CRC Press, 2002, pp. 220-228.

Chapter 5 Very High Energy Density Silicide-Air Primary Battery

5.1 Introduction

Continued efforts in the discovery and development of new material systems are critical to meeting the ever increasing demands for mobile power supply of our future society.[1-10] In general, in order to identify an optimal anode material, several basic considerations should be taken into account. First, it must promise sufficient theoretical energy density; second, it must consist of earth abundant and potentially low cost elements; third, it must be environmentally friendly; fourth, it should be conductive; and fifth, it must have a high redox potential for high operation voltage.[11-27] Based on these requirements, metal silicides represent an attractive class of materials with several unique features including high electron capacity, high conductivity and high operating voltage (with a theoretical maximum full cell voltage up to 1.9-2.5 V), high earth abundance and potential environmental benignity that are not readily simultaneously achievable in other competing material systems.

5.2 Results and Discussion

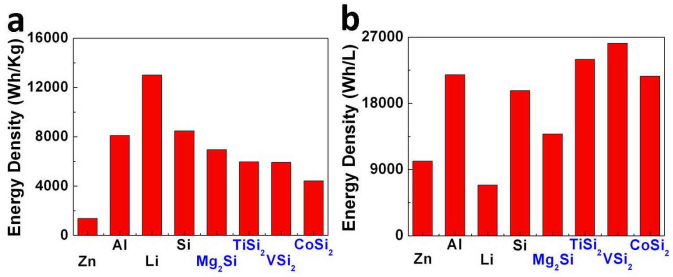

Figure 5.1 Theoretical gravimetric (a) and volumetric (b) anode energy density plot for air batteries. The calculation of volumetric energy density is shown in supporting information.

Figure 5.1a shows the theoretical gravimetric energy density of a few representative silicide materials along with Zn, Al, Li and Si. Silicide materials generally exhibit significant higher gravimetric energy density than Zn, the only commercialized metal-air battery system to date. Beyond the gravimetric energy density, volumetric energy density is another (and probably more) important figure of merit to consider, particularly important in a system with limited space. It should be noted that the theoretical volumetric energy density of some silicide materials (e.g. ~26,000 Wh/L for VSi_2) are 2-4 times higher than that of Zn (~10,150 Wh/L) or Li (~ 6,890 Wh/L) (Figure 5.1b). Additionally, most of the consisting elements of these metal silicides are abundant on earth and environmentally friendly, making them highly attractive for mobile power applications.

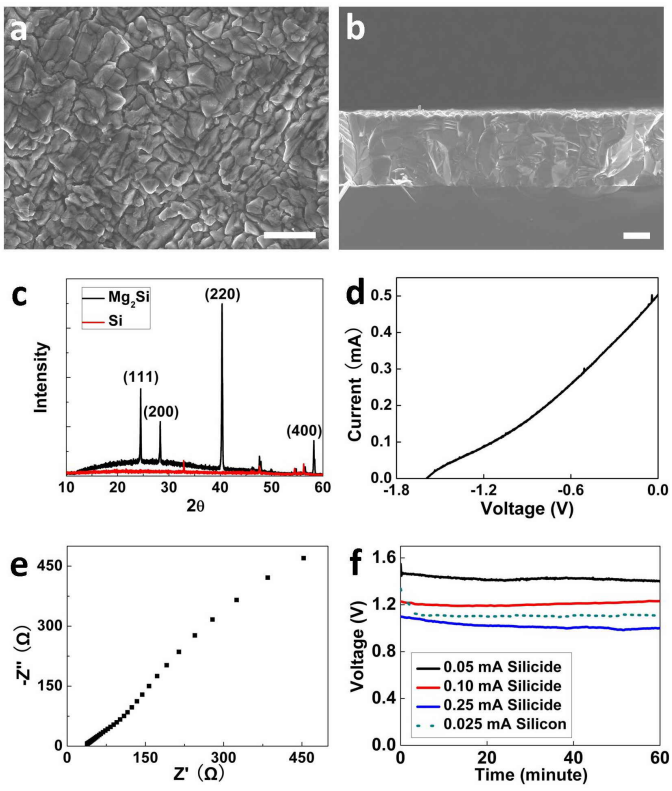

Figure 5.2 Characterization of magnesium silicide thin film. (a) Top view SEM image of Mg_2Si thin film on the silicon wafer. (b) Cross sectional SEM image of Mg_2Si thin film on the silicon wafer. (c) X-ray

Diffraction (XRD) patterns of Mg_2Si on the silicon wafer. (d) Linear sweep voltammograms of Mg_2Si thin film. (e) Electrochemical impedance spectroscopy of Mg_2Si thin film. (f) Galvanostatic discharge curve of Mg_2Si-air or Si-air battery in 30 % KOH solution with various discharge current. The scale bars in a and b are 10 μm.

In our initial studies, we have prepared the silicide films on the silicon wafer to investigate the performance of selected silicide-air battery system. We used the Mg_2Si system as an initial proof of concept system because of its easy preparation, highest theoretical voltage (up to 2.5V, see supporting information), and gravimetric energy density among all the silicide-air systems. The Mg_2Si thin film was obtained by reacting silicon wafer with magnesium vapor in a 12-inch horizontal tube furnace at 650°C for 60 minutes. Figures 5.2a and 5.2b show top view and cross sectional SEM images of Mg_2Si grown on the silicon wafer. The as-grown silicide displays a rough surface and a thin film with approximately 29 mm in thickness. X-ray Diffraction (XRD) studies demonstrate that silicide layer can be indexed to the pure cubic structure of Mg_2Si (Figure 5.2c).

To further investigate the electrochemical characteristics of the Mg_2Si thin film anode, linear sweep voltammograms and electrochemical impedance spectroscopy (EIS) were performed. The anodic dissolution potentials for Mg_2Si is -1.6 V (Figure 5.2d), demonstrating a high open circuit voltage for Mg_2Si-air battery. Figure 5.1e shows the impedance study of Mg_2Si thin film at a potential of 0.2 V. The Nequist plot at high frequency region normally reflects the equivalent series resistance (ESR) of the system. The intercept with real axis is estimated to be 38 Ω, implying a relatively low electrical resistance of the electrode material.[28] The galvanostatic discharge was then carried out with Mg_2Si as anode (Figure 5.2f). Consistent with the high anodic dissolution potential, the battery showed a rather high operating voltage under various

discharge current: 1.45 V at 0.05 mA, 1.21 V at 0.1 mA and 1.01 V at 0.25 mA. The performance of this thin film silicide battery is more efficient compared to the silicon battery that can only be continuously discharged under much lower current (see Figure 5.2f for example, the current of Si-air system is about 10 times smaller than that of Mg_2Si-air system at a similar discharge voltage for a similar sized device).[23] Although the operating voltage (1.45 V) is still lower than the theoretical number (~ 2.5 V, see supporting information), it is significantly higher than that in silicon-air couple (~1.1 V).[24] The relatively low operating voltage compared to the theoretical value is attributed to the self-discharge and the subsequent polarization of the electrode, similar to the case of Al–air system.

For practical applications, bulk mesh-powders are favored because of its possibility for scalable manufacturing along with other experimental advantages such as low cost and easy assembly. To this end, we have used commercially available silicide powder materials to make silicide pellets as anode. A typical polarization curve for titanium silicide ($TiSi_2$) in 30 % potassium hydroxide (KOH) solution is shown in Figure 5.3a (black curve). A potential of 1.35 V could be expected in the half-cell experiment. A very large current can also be observed (e.g. 90 mA maximum current for $TiSi_2$ pellet in Figure 5.3a vs. 0.5 mA for Mg_2Si thin film in Figure 5.2d), which may be attributed to the high conductivity of the metallic $TiSi_2$ and larger surface area in powder format. Unlike many other multi-electron anode materials,[27] no obvious corrosion (e.g. bubbling) was noticed when the $TiSi_2$ pellet was submerged in the KOH electrolyte, indicating a mild self-discharge characteristic that can promise a high practical capacity. Figure 5.3b shows a discharge measurement with different currents for $TiSi_2$ pellet. A voltage of ~1.28 V can be observed under slower discharge rates. Excitingly, the battery system can maintain a

stable voltage as high as 1.1 V under 3 mA discharge current and 1.15 V under 1 mA (Figure 5.3c).

A capacity measurement is also conducted with a full battery consisting of a $TiSi_2$ anode, an air electrode cathode and gel electrolyte.[23,29] A full discharge profile (black curve in Figure 5.3d) using 1 mA discharge current shows that a flat voltage plateau can be maintained at ~1.1 V, consistent with the results shown in Figure 5.3b and 5.3c. Evident in the curve, a capacity of ~1,800 mAh/g is experimentally achieved, which is close to 60 % of the theoretical capacity based on the anode reaction.

To further investigate the electrochemical behaviour of silicide family, we have conducted parallel experiments for VSi_2, $CoSi_2$ and Mg_2Si pellets, which also promise high theoretical energy densities. With a slightly lower voltage and current, VSi_2 and $CoSi_2$ show similar behaviour in the polarization curve (Figure 5.3a). In addition, both VSi_2 and $CoSi_2$ can sustain a voltage of ~0.85 and ~0.9 V for extended periods of time at a discharge current of 1 mA (Figure 5.3b, 5.3c). The capacity measurements show that the VSi_2 and $CoSi_2$ exhibit an un-optimized practical capacity for 1,500 mAh/g and 1,300 mAh/g, respectively (Figure 5.3d). On the other hand, although Mg_2Si has a relatively high voltage, it cannot sustain discharge under high current (Figure 5.3b), which is consistent the thin film case (Figure 5.2f). Based on our experimental results, $TiSi_2$ not only has a higher open circuit voltage, but also offers a higher potential under high discharge current among all silicides studied.

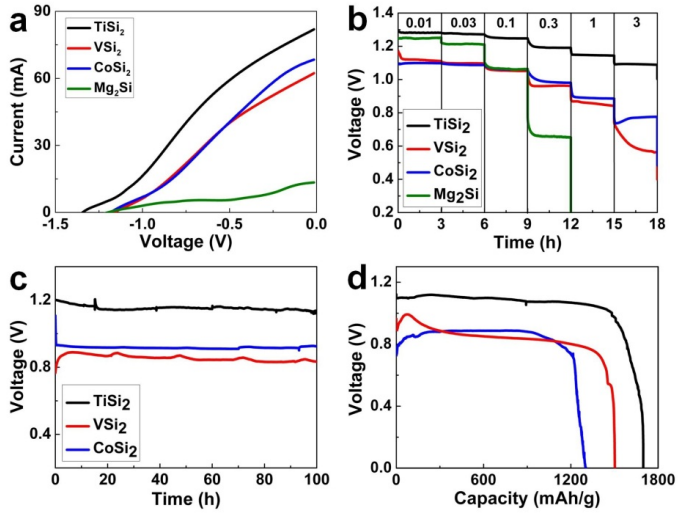

Figure 5.3 Electrochemical performance for silicide-air batteries. (a) Polarization curves for silicide pellets in 30 % KOH solution. (b) Discharge curves for silicide pellets with different discharge currents (mA). (c) Discharge curves for $TiSi_2$, VSi_2 and $CoSi_2$ pellets at a discharge rate of 1 mA. (d) Capacity measurements for $TiSi_2$, VSi_2 and $CoSi_2$ powders at a discharge current of 1 mA.

Together, we have reported a novel group of silicide-air primary batteries and demonstrated that silicide-air batteries can promise a new metal-air battery system with unparalleled energy density. Several intrinsic features of silicide materials, including high electron capacity, high conductivity, high operating voltage, high earth abundance and potential environmental benignity, make them an excellent class of materials for high density energy storage. In particular, the $TiSi_2$ offers a higher anode capacity than any other types of anode on both the gravimetric and volumetric scale (Figure 5.4a, 5.4b). For example, the volumetric anode capacity of $TiSi_2$ can reach ~ 7230Ah/L, which is over 7 fold of that for Al-air system (Altek Fuel Group Inc. model APS 100–12, capacity 120Ah, Al anode 0.37kg).[19]

For many practical applications with limited space or mass loading capacity, both gravimetric and volumetric energy densities are important metrics to consider. To properly evaluate both scales with a single unit, we propose to use the product of gravimetric and

volumetric energy density to define a new figure of merit for energy density – gravolumetric energy density. The reciprocal of this number also carries an important physical meaning – the product of mass and volume of the material needed to generate a unit of energy (e.g. W·h). It therefore defines a parameter that characterizes the required mass and volume of a chosen material to provide a given amount of energy. A well-developed metal-air system typically have an active anode material weight ratio of about 40% of their total battery weight.[13,14] Therefore, we have projected the gravolumetric energy density of the silicide system based on this ratio, the practical anode capacity (Figure 5.4a, 5.4b) and the operating voltage and compared with the practical gravolumetric energy density of Zn-[13] and Al-air system (Altek Fuel Group Inc. model APS 100–12, specific energy ~300Wh/kg).[19] With this new figure of merit, our silicide system offers significant combined advantages over any other more mature metal-air technologies, with the practical gravolumetric energy density of $TiSi_2$-air system more than 3-10 times better than that of Zn-air or Al-air technologies (Figure 5.4c).

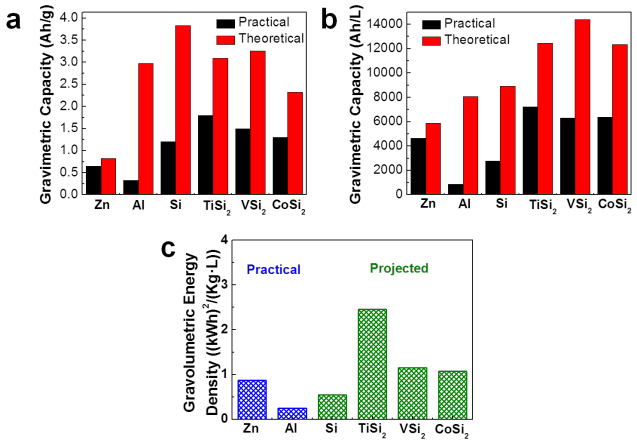

Figure 5.4 (a) Gravimetric and (b) volumetric anode capacity for various anode materials (c) gravolumetric energy density plot of the practical values (blue) obtained in Zn-air battery, Al-air battery and the projected values (green) in Si-air battery or silicide-air batteries.

5.3 Conclusions

Together, we have reported a novel group of silicide-air batteries and demonstrated the utilizing of silicide family materials as anode in the primary metal-air battery system with unparalleled anode capacity. Several intrinsic features of silicide materials, including high electron capacity, high conductivity, high operating voltage, high earth abundance and potential environmental benignity, make them an excellent class of materials for ultra-high density energy storage. With the high intrinsic conductivity of metal silicides, conductive materials such as carbon black will no longer be needed in our system, which ensures high energy density in practical usage. Additionally, many of these silicide materials are generally consisted of earth abundant and environmentally friendly elements to promise sustainable lower cost manufacturing. For example, comparing earth abundance of constituting elements of $TiSi_2$ with the current (Zn) or emerging (Al, Li) potential competing air battery anode materials, Si (270,000 ppm) is more than 3 time richer than Al (82,000 ppm) and about 3-4 orders of magnitude richer than Zn (79 ppm) and Li (17 ppm), and Ti (6,600 ppm) is about 2-3 orders of magnitude richer than Zn and Li. In the long run, with the development of tri-electrode cell configuration and highly efficient oxygen reduction/evolution reaction catalyst,[30] secondary silicide air may also be envisioned with superior anode capacity and high practical energy density. Therefore, silicide materials such as $TiSi_2$ are posed to be a very strong contender for future energy storage. With further optimization and process development, silicide material can enable a new battery family with ultra-high energy density and open up exciting opportunities for future mobile power applications.

5.4 Materials and Method

Magnesium silicide thin film fabrication and measurement. Magnesium silicide thin films were synthesized in a 12-inch horizontal tube furnace (Lindberg/Blue M, Thermo Scientific)with a 1-inch diameter quartz tube. An n-type silicon wafer with resistivity of 0.001-0.002 Ω·cm (University Wafers) was put on the top of an alumina boat filled with magnesium powder (99.8 %, Alfa Aeser). The alumina boat was then placed in the center of the furnace. Finally, the chamber was heated to 650 ^{o}C under argon flow for 1 hour followed by natural cooling to room temperature to obtain a silicon substrate with a layer of blue silicide thin film (~45μm thick).

Magnesium silicide thin film electrochemical performance measurement. The battery device consisting of a silicide thin film with a film thickness around 45 μm on the silicon wafer (~1.5 cm × 2 cm, 500 μm thick), an air diffusion electrode (Quantumsphere Co. Ltd) and a PDMS stamp with an open-through hole (~0.5 cm diameter) was sandwiched tightly by aluminum sheet and plastic plate with open windows at the center of the air electrode to allow air diffusion. An aqueous solution of 30 % potassium hydroxide (KOH) was then injected into the cell as the electrolyte.

Silicide pellet electrochemical performance measurement. 1.5 g of $TiSi_2$ (99.5 %), $CoSi_2$ (99%) and VSi_2 (99.5%) and ~0.7g of Mg_2Si (99.5%) powders (Alfa Aeser) were pressed to form pellets with ~0.5 inch in diameter and ~0.25 cm in height (29) and annealed under argon flow for 2 h at different temperatures (1,100 ^{o}C for $TiSi_2$ and VSi_2, 900 ^{o}C for $CoSi_2$, 700 ^{o}C for Mg_2Si). Discharge measurements were then carried out with the silicide pellet as anode, an air diffusion electrode as cathode and 30 % potassium hydroxide (KOH) as the electrolyte.

Silicide powder capacity measurement. For the capacity measurement, a gel was made by adding poly-acrylic acid (Carbopol 711, BF Goodrich) into KOH solution. The gel was then casted onto a nickel foil (0.025 mm thick, Alfa Aesar) with silicide powder. A full cell is

constructedsimilarly except that the silicon wafer was substituted with the silicide pasted nickel foil with a separator (Celgard 3501) on the top.

Characterization. All the discharge curves were achieved using a Maccor 4304 battery test system. Linear sweep voltammograms and electrochemical impedance spectroscopy were performed with a 3-electrode configuration on VersaSTAT 4 from Princeton Applied Research. The as-synthesized magnesium silicide thin films were characterized by scanning electron microscopy (SEM JEOL 6700) and Energy-dispersive X-ray spectroscopy. X-ray Diffraction(XRD) pattern was carried out by a Bruker Smart 1000K Single Crystal X-ray Diffractometer.

5.5 Bibliography

1. S. Xu, Y. Qin, C. Xu, Y. G. Wei, R. Yang, Z. L. Wang, *Nat. Nanotech*. 2010, 5, 366-373.
2. B. Tian, X. L. Zheng, T. J. Kempa, Y. Fang, N. F. Yu, G. Yu, J. Huang, C. M. Lieber, *Natur*e., 2007, 449, 885-888.
3. A. I. Hochbaum, P. D. Yang, Chem. Rev. 2010, 110, 527-546.
4. P. Simon, Y. Gogotsi, *Nat. Mater*., 2008, 7, 845-854.
5. H. L. Zhao, Y. Li, Z. M. Zhu, J. Lin, Z. H. Tian, R. L. Wang, Electrochim. Acta., 2008, 53, 7079-7083.
6. Y. K. Sun, S. T. Myung, B. C. Park, J. Prakash, I. Belharouak, K. Amine, *Nat. Mater*., 2009, 8, 320-324.
7. J. B. Goodenough, Y. Kim, *Chem. Mater*., 2010, 22, 587-603.
8. H. L. Wang, L. F. Cui, Y. Yang, H. S. Casalongue, J. T. Robinson, Y. Liang, Y. Cui, H. J. Dai, *J. Am. Chem. Soc*., 2010, 132, 13978-13980.
9. S. Chen, J. W. Zhu,X. D. Wu, Q. F. Han, X. Wang, *ACS Nano*, 2010, 4, 2822-2830.

10. P. Banerjee,I. Perez, L. Henn-Lecordier, S. B. Lee,G. W. Rubloff, *Nat. Nanotech.,* 2009, 4, 292-296.
11. F. Y. Cheng, J. Chen, *Chem. Soc. Rev*., 2012, 41, 2172-2192.
12. M. Armand, J. M. Tarascon, *Nature.,* 2008, 451, 652-657.
13. G. Girishkumar, B. McCloskey, A. C. Luntz, S. Swanson, W. Wilcke, *J. Phys. Chem. Lett*., 2010, 1, 2193-2203.
14. http://data.energizer.com/PDFs/alkzincairnomercury_psds.pdf
15. C. Chakkaravarthy, A. K. A. Waheed, H. V. K. Udupa,. *J. Power Sources,* 1981, 6, 203-228.
16. V. Neburchilov, H. J. Wang, J. J. Martin, W. Qu, *J. Power Sources,* 2010, 195, 1271-1291.
17. Y. Hori, J. Takao, H. Shomon, *Electrochim. Acta*., 1985, 30, 1121.
18. C. S. Li, W. Q. Ji, J. Chen, Z. L. Tao, *Chem. Mater.,* 2007, 19, 5812 – 5814.
19. http://www.altekfuel.com/userfiles/File/SDS_APS100_12-24_V-04.pdf
20. P. G. Bruce, L. J. Hardwick, K. M. Abraham, *MRS Bull.,* 2011, 36, 506-512.
21. P. G. Bruce, S. A. Freunberger, L. J. Hardwick, J. M. Tarascon, *Nat. Mater.,* 2012, 11, 19-29.
22. J. Christensen, P. Albertus, R. S. Sanchez-Carrera, T. Lohmann, B. Kozinsky, R. Liedtke, J. Ahmed, A. Kojic, *J. Electrochem. Soc*., 2012, 159, R1-R30.
23. X. Zhong, H. Zhang, Y. Liu, J. W. Bai, L. Liao, Y. Huang, X. F. Duan, *Chem. Sus. Chem*., 2012,5, 177-180.
24. G. Cohn, D. Starosvetsky, R. Hagiwara, D. D. Macdonald, Y. Ein-Eli, *Electrochem. Commun.,* 2009, 11, 1916-1918.
25. H. X. Yang, Y. D. Wang, X. P. Ai, C. S. Cha, *Electrochem. Solid-State Lett.,* 2004, 7, A212-A215.

26. S. Licht, H. M. Wu, X. W. Yu, Y. F. Wang, *Chem. Commun.,* 2008, 28, 3257-3259.

27. T. N. Lambert, D. J. Davis, S. J. Limmer, M. R. Hibbs, J. M. Lavin, *Chem. Commun.,* 2011, 47, 9597-9599.

28. G. H. Yu, L. B. Hu, N. Liu, H. L. Wang, M. Vosgueritchian, Y. Yang, Y. Cui, Z. N. Bao, *Nano Lett.,* 2011, 11, 4438-4442.

29. H. Zhang, Y. N. Zhou, Q. Sun, Z. W. Fu, *Solid State Sci*., 2008, 10, 1166-1172.

30. Y. G. Li, M. Gong, Y. Y. Liang, J. Feng, J. E. Kim, H. L. Wang, G. S. Hong, B. Zhang, H. J. Dai, *Nature Commun*., 2013,4, 1085.

Chapter 6 Graphene Membrane Cathode for high Energy Density Rechargeable Lithium-air Batteries in Ambient Conditions

6.1 Introduction

Lithium-air batteries with aprotic electrolytes have garnered intensive interest for mobile energy supplies because of its potential to offer an energy density far exceeding that of lithium-ion batteries and other energy storage systems[1-8]. Despite this exciting potential, practical implementation of Li-air batteries is a considerable challenge, particularly with the electrolyte and air cathodes[9-13]. Cathode materials such as nanoporous gold[14], TiC[15], carbon nanotube[16] have been explored for optimizing the battery capacity and cycle life. Most studies to date have been focusing on Li-air batteries operation under pure oxygen conditions. However, the operation of Li-air batteries under ambient conditions is more relevant for practical applications and is considerably more challenging. The Maxpower group has shown that Li-air batteries operate significantly different in ambient conditions than in a pure oxygen enviroment[17,18]. The low oxygen partial pressure in air can limit O_2 accessibility to the cathode. Thus, it is desirable to have a cathode electrode that is highly porous for fast oxygen diffusion and also with a high specific surface area for efficient charge/discharge cycles. Additionally, the water moisture in ambient air can react with the discharge product (Li_2O_2) and/or even corrode the Li anode to sabotage the inner systems of the battery and severely undermine the battery stability and cycling endurance[19]. A Li-air battery with a cathode composed of SWNTs and ionic liquid in gel has been reported with 100 cycles under ambient conditions[20], which however requires a high charge over-potential (charge voltage > 5 V) because of formation of undesired discharge product ($LiOH/Li_2CO_3$) without moisture protection[21].

In general, an ideal air-cathode should satisfy several basic requirements in order to ensure stable and reversible operations of high energy density Li-air batteries under ambient conditions. First, the cathode should consist of a highly interconnected conducting network to ensure efficient charge transport even after the deposition of the insulating discharge product (Li_2O_2). Second, the cathode should have a large surface area for higher surface deposition capacity of the discharge product and for efficient oxygen reduction reaction under low oxygen partial pressure. Third, a hierarchical porous structure is desired for efficient diffusion of electrolyte ions and oxygen. Lastly, hydrophobic and moisture resistive characteristics are desired for O_2/H_2O selectivity and retarding moisture diffusion for improved cycling stability and endurance under the ambient conditions.

Graphene, a single atomic layer sheet of graphite, has been recently explored as Li-air battery electrode due to its excellent electrical conductivity and high surface area[22-25]. Additionally, it has been suggested that the defects and functional groups on the reduced graphene oxide can act as catalytic active sites for both oxygen evolution reaction (OER) and oxygen reduction reaction (ORR) that are essential for the charge/discharge processes[26-30]. Yoo reported graphene sheets as air electrodes with a hybrid electrolyte, and demonstrated that the sp^3 bonding from edge and defect sites showed considerable catalytic activity in reducing and evolving oxygen[29]. Wang proposed a hierarchically porous carbon cathode, and reached stable primary discharge performance (11,060 mAh/g) under oxygen, but with limited cycle life (~2000 mAh/g for 10 cycles) in secondary performance[28]. Xiao reported a hierarchically porous graphene cathode and achieved high primary capacity of 15,000 mAh/g in oxygen, but only ~5000 mAh/g in ambient air[27]. Moreover, binders such as Polyvinylidene fluoride (PVDF) were generally adopted in cathode but found to be chemically reactive with potential discharge

product (e.g. LiO_2, Li_2O_2, LiOH), resulting in the product degrading upon cycling.[31-33]

Here we propose a binder-free hydrophobic and densely packed three-dimensional (3D) graphene membrane as an effective cathode for the stable and reversible operation of Li-air batteries under ambient conditions. We demonstrate that the 3D graphene membrane allows for efficient transport of charges, electrolyte ions and oxygen, and high capacity storage of insulating discharge product, thus enabling a Li-air battery with exceptional performance, including a highest capacity exceeding > 5700 mAh/g (up to 20 cycles) and excellent cycling behaviour (>100 cycles at 1400 mAh/g and >2000 cycles at 140 mAh/g), with a lifespan capacity of 100,000-300,000 mAh/g, comparable to that of lithium ion battery cathode.

6.2 Results and Discussion

The 3D graphene membrane exhibits several unique characteristics making it an excellent air cathode material (Figure 6.1). First, the high surface area 3D conducting network structure can ensure high capacity deposition of the insulating discharge product Li_2O_2 without affecting the intrinsic charge transport properties of the cathode. Second, the highly porous network structure can offer highly efficient diffusion pathways for oxygen and electrolyte ions. Third, the high specific surface area can offer plentiful active sites for ORR and OER for efficient charge/discharge processes. Moreover, the highly tortuous, hydrophobic, densely packed architecture can generate O_2/H_2O selectivity, effectively retard the moisture diffusion and reduce the adverse impact of moisture under ambient conditions. Lastly the graphene skeleton structure not only avoids the introduction of conventional binder, preventing the potential chemical instability, but also may provide possible thermal conducting channels, avoiding localized heating. Together, these unique attributes of the proposed graphene membrane cathode can enable a high capacity Li-air battery with stable cycling performance in both oxygen and ambient

conditions.

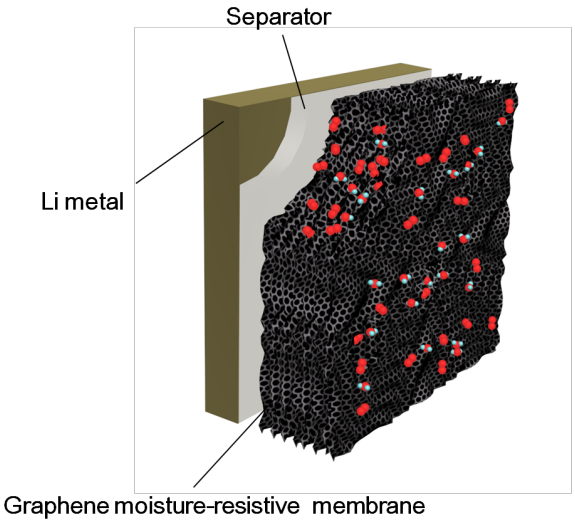

Figure 6.1 A scheme of the Li-air battery configuration with a Li metal anode, separator and graphene moisture-resistive membrane cathode.

A commercially available carbon paper was used as support for the graphene membrane cathode (Figure 6.2a). Graphene oxide (GO) was prepared by modified Hummer's method[24,25]. A concentrated GO solution (4.0~8.0 g/L) was prepared and uniformly coated onto the carbon paper, and freeze-dried to obtain a 3D porous GO membrane (Figure 6.2b). The GO was reduced to graphene by annealing in an argon atmosphere at 400 ^{o}C, as indicated by the colour change from deep yellow into dark grey (Figure 6.2c). The resulting graphene membrane on carbon paper was then compressed and cut into round disks to create air-cathode electrodes for coin cells. Figure 6.2d shows a typical scanning electron microscope (SEM) image of the as-prepared graphene thin membrane on the carbon paper. The thickness and the density of the graphene membrane can be readily tuned for various stability, energy and power requirements.

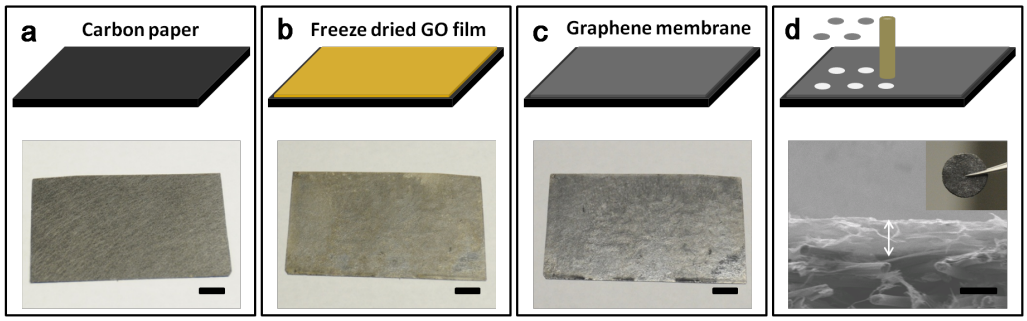

Figure 6.2 A scheme of scalable preparation of the graphene membrane cathode. (a) Commercial carbon paper (b) Graphene oxide coated on the carbon paper. (c) Graphene membrane formed after annealing (d) Membrane cut into round shaped disks for battery assembling and cross sectional SEM image of graphene membrane cathode. Scale bars are 1 cm in a,b,c and 20 μm in d.

The coin cells assembled with 3D graphene membrane air cathode were first characterized by a galvanostatic discharge/charge process in pure oxygen (black curve in Figure 6.3a). The discharge voltage for the graphene membrane cathode is 2.71 V while the charging process shows a flat platform around 3.54 V. A similar test conducted under ambient conditions demonstrates a highly similar behaviour with only a slight decrease in discharge voltage (2.67 V) and slight increase in charge voltage (3.59 V) (red curve in Figure 6.3a).

We have further conducted multiple charge/discharge cycles in both oxygen and ambient conditions to evaluate the cycling endurance of the graphene membrane cathode. As a control experiment, we first tested a carbon black based air cathode, which exhibits expected performance in oxygen with little charge polarization (black curve in Figure 6.3b top), consistent with the previous report[11]. However, when operating under ambient conditions (red curve in Figure 6.3b top), significant voltage polarization is observed within the first few cycles and with the charge voltage quickly climbing up to 4.2 V where the electrolyte will undergo irreversible decomposition. The charging polarization is normally correlated to the inefficient/incomplete

decomposition of Li_2O_2 during the oxygen evolution process. The severe polarization observed in carbon black cathode under ambient conditions is largely attributed to the moisture in the air, which could react with Li_2O_2 and form non-rechargeable side-products (e.g. LiOH)[34]. Additionally, upon deep charge/discharge cycling and accumulation of side-products, the carbon black particles may disintegrate and lose electrical connection with its surroundings. Excitingly, the graphene membrane cathode shows highly stable charge and discharge characteristics over multiple cycles with little voltage polarization in both pure oxygen (black curve in Figure 6.3b bottom) and ambient conditions (red curve in Figure 6.3b bottom), suggesting that most of the Li_2O_2 fully converted even under ambient conditions, which may be attributed to its highly interconnected 3D conducting network and effective retardation of moisture diffusion by the hydrophobic dense membrane structure.

We have further conducted X-ray diffraction (XRD) studies to analyze the discharge product (Figure 6.3c). The discharged cathode under ambient conditions displays diffraction peaks at 33^o, 35^o, 41^o, which are absent from both the pristine and recharged graphene cathodes. This discharge product can be indexed as Li_2O_2, consistent with previous reports[11]. We have further used SEM studies to evaluate the graphene cathode at pristine, discharged and re-charged state. The pristine graphene membrane electrode shows a relatively clean, densely packed surface and tortuous channels (Figure 6.3d). In the discharged state, a large amount of Li_2O_2 particles are clearly seen on the graphene membrane (Figure 6.3e), consistent with the XRD studies. It also demonstrates that after discharge, the graphene cathode is able to retain its dense 3D interconnected porous network, therefore ensuring electrical conductivity of the graphene network, and sufficient room for oxygen and electrolyte ion diffusion during the charging and discharging processes. Upon recharge, almost all the particles disappear from the graphene

membrane (Figure 6.3f), suggesting a complete recharge of Li_2O_2.

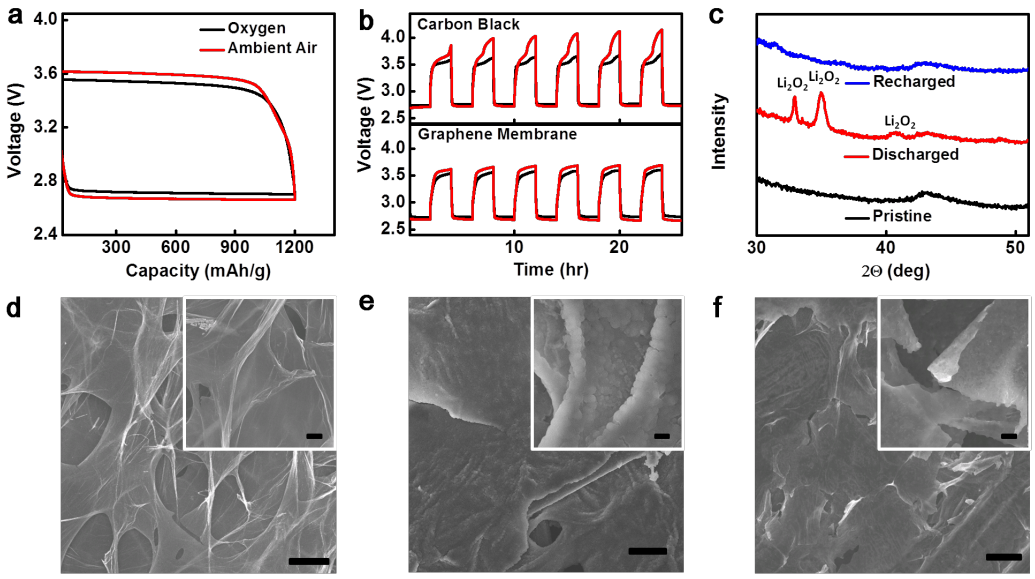

Figure 6.3 Graphene membrane cathode based Li-air cell performance and cathode analysis in ambient air. (a) Galvanostatic discharge/charge curve for 20 µm graphene membrane cathode based Li-air cell in oxygen and ambient conditions. (b) Galvanostatic cycling of carbon black cathode based Li-air cell (top) and graphene membrane cathode based Li-air cell (bottom) in pure oxygen (black) and ambient air (red). (c) XRD analysis of a pristine graphene cathode, a discharged graphene membrane cathode and a recharged graphene cathode. SEM image of (d) pristine, (e) discharged and (f) recharged graphene cathode. Scale bars are 10 µm and 2 µm (inset).

The stable operation of Li-air batteries under ambient conditions has typically been a challenge. Water vapour is generally believed to be the main factor responsible for the poor cycling characteristics of Li-air batteries under ambient conditions[17,18]. To this end, an oxygen selective membrane may be adopted to allow the diffusion of oxygen while slowing down the ingression of water vapour. A primary battery has been demonstrated with a protective oxygen selective membrane by Maxpower group[17]. However, no rechargeable behaviour was reported.

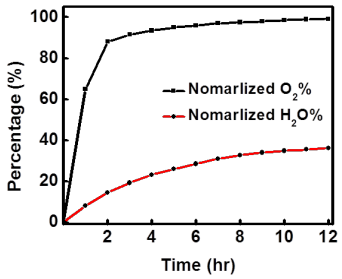

Figure 6.4 Moisture and oxygen diffusion behaviour through the graphene membrane. Normalized oxygen diffusion rate (black) and normalized moisture diffusion rate (red) over a highly dense graphene membrane (~20 μm).

For an ideal air cathode electrode working in ambient conditions, the cathode should allow efficient oxygen diffusion while effectively retarding moisture diffusion as much as possible. In general, the molecule transmission through the graphene membrane can be attributed to both the Knudsen diffusion, dictated by membrane geometric parameters (e.g. pore size, density, tortuosity etc.), and the surface diffusion, determined by the molecule-graphene interaction[35]. Knudsen diffusion can be tuned by creating a thicker or denser graphene membrane. However it is not tuneable for gas molecule selectivity. Surface diffusion may be engineered to create a membrane that may allow selective oxygen diffusion but with limited rate. Specifically, on the hydrophobic graphene surface, the chemisorbed oxygen molecule can migrate from one site to another through surface diffusion mechanism[35]. However, water molecules tend to form clusters or even ice crystalline domains on hydrophobic graphene surfaces with little surface diffusion effect[36-38]. Therefore, the surface diffusion of oxygen molecules on hydrophobic graphene is significantly greater than that of water molecules, resulting in an effective O_2/H_2O selectivity[39-41].

In practice, a balanced approach has to be taken. An adequate Knudsen diffusion rate and

O_2/H_2O selectivity would be both required to create a membrane barrier layer that can sustain sufficient air flow while retaining the O_2/H_2O selectivity for battery operation under ambient conditions. To validate this hypothesis, we have conducted water and oxygen permeability tests through the graphene membrane, which clearly shows a much slower diffusion of water molecules than oxygen molecules (Figure 6.4). After 10 hours, the moisture concentration increases very slowly and becomes almost saturated at ~35 % of ambient conditions (~17.8 ^{o}C, ~52.5% relative humidity). At the same time, the oxygen shows a much faster diffusion from the beginning and reaches equilibrium with outer atmosphere (100%) after 5 hours. Lower moisture penetration can surely be expected with a denser/thicker graphene membrane[19], but this could also slow down the oxygen diffusion rate (much lower Knudsen diffusion rate within denser/thicker membrane) and degrade the discharge current. From a full cell perspective, moisture penetration rate can be further tuned with cell configuration, size of gas holes, hydrophobicity of carbon paper etc. Together, these studies demonstrate that the diffusion rate and O_2/H_2O selectivity can be tuned to meet specific application needs by designing a graphene moisture-resistive membrane with a controlled membrane density and thickness.

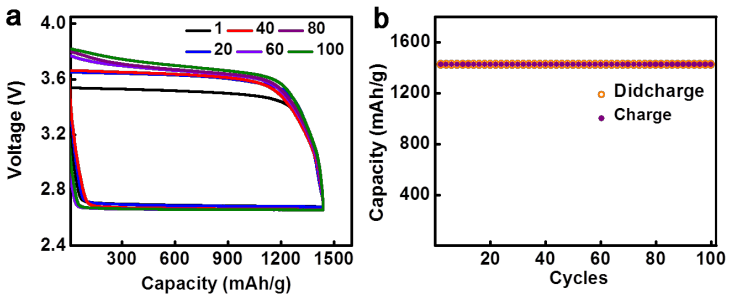

Figure 6.5 Capacity-limited test. (a) Galvanostatic cycling of a Li-air cell with a 20 μm graphene membrane cathode under a capacity limitation of ~1425 mAh/g. (b) Cycling profiles under a capacity limitation of ~1425 mAh/g in ambient air. Current rate is 2.8 A/g.

To evaluate the cycling stability of our Li-air batteries under ambient conditions, we have cycled the device at different charge/discharge capacities. The Li-air battery is first cycled with a moderate capacity of 1425 mAh/g (Figure 6.5a). Excitingly, the device displays a highly stable cycling behaviour up to 100 cycles with nearly the same charge/discharge behaviour for each cycle (Figure 6.5b). After 50 cycles, the charge over-potential begins to gradually increase and reaches 3.8V at 100 cycles. To further evaluate the operation stability at a deeper discharge state, we have conducted cycling tests at a capacity of 2850 mAh/g and 5700 mAh/g (Figure 6.6a,b). Discharge capacity is readily achieved with little charge polarization for 50 cycles (Figure 6.6d) and 20 cycles (Figure 6.6e) respectively.

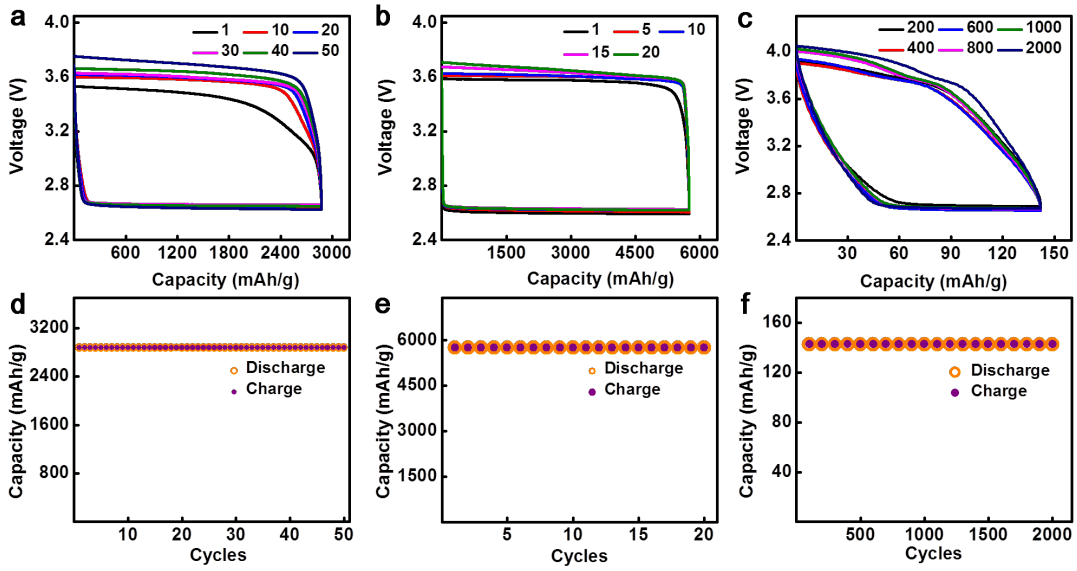

Figure 6.6 Capacity-limited test at variable capacities. Galvanostatic cycling of Li-air cells with a 20 µm graphene membrane cathode under a capacity limitation of (a) ~2850 mAh/g, (b) ~5700 mAh/g, and (c) ~140 mAh/g. Cycling profiles under a capacity limitation of (d) ~2850 mAh/g, (e) ~5700 mAh/g (f) ~140 mAh/g in ambient air. Current rate is 2.8 A/g.

Although the graphene membrane air cathode has exhibited stable cycling performance up

to 100 cycles, the cycle life is still far from a Li-ion battery cathode, which is typically over 1000 cycles. It is important to note that our graphene membrane air cathode capacity (1400-5700 mAh/g) greatly exceeds that of Li-ion batteries (120~150 mAh/g) by 10-40 times. Therefore, the lifespan cathode capacity (single discharge capacity × cycle number) of the graphene membrane air-cathode is on par with a typical Li-ion battery cathode. With comparable lifespan capacity but much higher single charge capacity, the Li-air battery with graphene membrane air cathode may offer a unique energy storage solution that can greatly increase the battery life (by >10 times) and reduce the frequency of charge cycles, bridging the gap between rechargeable Li-ion batteries and traditional primary batteries. Moreover, by reducing the degree of discharge (lower capacity per cycle), it is also possible to achieve much longer cycle life while holding a capacity comparable to that of Li ion battery cathode. For example, we have performed a cycling test at a capacity of ~140 mAh/g and achieved stable operation over 2000 cycles, which is comparable to a Li-ion battery cathode (Figure 6.6c,f).

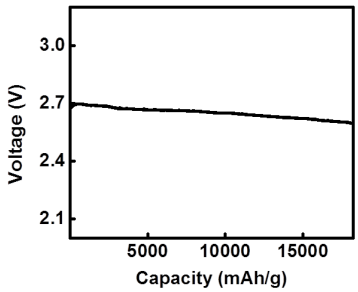

Figure 6.7 Li-air primary application. Galvanostatic discharge curve of a graphene membrane cathode based Li-air cell for 90 hours. Current rate is 0.2 A/g.

Lastly, we have also performed a single discharge on the graphene membrane cathode under ambient conditions and cut off the discharge at 2.6 V. The battery discharges for over 90 hours and delivers a cathode capacity of more than 18,000 mAh/g (Figure 6.7), which is about 100

times higher than the cathode capacity of the primary Li-MnO_2 battery[42].

6.3 Conclusions

In summary, our studies demonstrate that a binder-free high capacity air cathode can be constructed using a hydrophobic dense 3D graphene membrane. The 3D graphene membrane structure has a highly interconnected graphene network for efficient charge transport, a highly porous structure for efficient diffusion of oxygen and electrolyte ions, a thermal-conductive channel for heat transfer and a large specific surface area for high capacity storage of the discharge product, Li_2O_2. Lastly, the highly tortuous hydrophobic graphene membrane generates O_2/H_2O selectivity and effectively retards moisture diffusion to ensure excellent charge/discharge cycling performance under ambient conditions. Together, these combined features allow us to create a Li-air battery with excellent cycling performance (over 100 cycles with 1425 mAh/g) and extremely high capacitance (over 5700mAh/g over 20 cycles). Our results demonstrate that a scalable, high capacity, long life cycles Li-air battery cathode can be achieved by rationally designing the graphene moisture-resistive membrane cathode. With exceptional high single charge capacity and comparable lifespan capacity to that of a Li-ion battery cathode, the graphene membrane air cathode opens up exciting new opportunities to bridge the gap between traditional rechargeable Li-ion batteries and primary batteries, greatly increasing the battery life and reducing the necessary recharge frequency to meet future challenges for mobile power supplies in diverse areas.

6.4 Materials and Method

Li-air cell assembling. All the cells were assembled in an argon-filled glove box with water and oxygen content kept both below 0.1 ppm. The positive top cover was machine-drilled to create

holes to enable gas diffusion. The cell consists of a metallic Li foil anode and the aforementioned graphene cathode with a commercial carbon paper as the current collector. A Celgard separator is used to separate the cathode from the anode. A solution of 1 M solution of lithium nitrate ($LiNO_3$) in N,N-dimethylacetamide (DMA) was used as the electrolyte.

Electrochemical measurement. For the test in pure oxygen, the as prepared Li-air cell was kept in a homemade glass chamber flooded with oxygen during testing. For operation in ambient conditions, the as prepared Li-air cell was directly tested in the ambient air. Galvanostatic discharge/charge was performed with Maccor 4340.

SEM and XRD analysis. Scanning electron microscopy (SEM JEOL 6700) was used to observe the morphology of the air cathode. X-ray Diffraction (XRD) pattern was carried out using Bruker Smart 1000K Single Crystal X-ray Diffractometer.

Oxygen and moisture diffusion test. The dense graphene membrane was prepared on a copper foil with ~0.5 mm hole in diameter, with the compressed graphene membrane fully covering the hole. A closed homemade chamber with oxygen/moisture sensor inside and the graphene membrane covered copper foil seal was assembled in the glove box. After exposing to ambient air, the change of oxygen/moisture inside the chamber was recorded as a function of time.

6.5 Bibliography

1. N. Lopez, D. J. Graham, Jr. R. McGuire, G. E. Alliger, S. H. Yang, C. C. Cummins, D. G. Nocera, *Science* 2012, 335, 450-453.

2. O. Crowther, B. Meyer, M. Morgan, M. Salomon, *J Power Sources* 2011, 196, 1498-1502.

3. H. Zhang, X. Zhong, J. C. Shaw, L. X. Liu, Y. Huang, X. F. Duan, *Energy Environ. Sci.* 2013, 6, 2621-2625.

4. F. J. Li, H. Kitaura, H. S. Zhou, *Energy Environ. Sci.* 2013, 6, 2302-2311.

5. A. Debart, A. Paterso, J. Bao, P. G. Bruce, *Angew. Chem. Int. Ed.* 2008, 47, 4521-4524.

6. S. S. Zhang, J. Read, *J Power Sources* 2011, 196, 2867-2870.

7. Y. C. Lu, H. A. Gasteiger, M. C. Parent, V. Chiloyan, S. H. Yang, *Solid State Lett.* 2010, 13, A69-A72.

8. X. Zhong, H. Zhang, Y. Liu, J. W. Bai, L. Liao, Y. Huang, X. F. Duan, *ChemSusChem* 2012, 5, 177-180.

9. H. G. Jung, J. Hassoun, J. B. Park, Y. K. Sun, B. Scrosati, *Nat. Chem.* 2012, 4, 579-585.

10. S. A. Freunberger, Y. H. Chen, N. E. Drewett, L. J. Hardwick, F. Bard, P. G. Bruce, *Angew. Chem. Int. Ed.* 2011, 50, 8609-8613.

11. W. Walker, V. Giordani, J. Uddin, V. S. Bryantsev, G. V. Chase, D. A Addison, *J. Am. Chem. Soc.* 2013, 135, 2076-2079.

12. B. D. McCloskey, R. Scheffler, A. Speidel, D. S. Bethune, R. M. Shelby, A. C. Luntz, *J. Am. Chem. Soc.* 2011, 133, 18038-18041.

13. G. Girishkumar, B. McCloskey, A. C. Luntz, S. Swanson, W. Wilcke, *J. Phys. Chem. Lett.* 2010, 1, 2193-2203.

14. Z. Q. Peng, S. A. Freunberger, Y. H. Chen, P. G. Bruce, *Science* 2012, 337, 563.

15. M. M. O. Thotiyl, S. A. Freunberger, Z. Q. Peng, Y. H. Chen, Z. Liu, P. G. Bruce, *Nat. Mater.* 2013, 12, 1050-1056.

16. Y. F. Li, Z. P. Huang, K. Huang, D. Carnahan, Y. C. Xing, *Energy Environ. Sci.* 2013, 6, 3339-3345.

17. O. Crowther, M. Salomon, *Membranes* 2012, 2, 216-227.

18. O. Crowther, D. Keeny, D. M. Moureau, B. Meyer, M. Salomon, M. Hendrickson, *J Power Sources* 2012, 202, 347–351.

19. J. Zhang, W. Xu, X. H. Li, W. Liu, *J. Electrochem. Soc.* 2010, 157, A940-A946.

20. T. Zhang, H. S. Zhou, *Nat. Commun.* 2013, 4, 1817.

21. H. K. Lim, H. D. Lim, K. Y. Park, D. H. Seo, H. Gwon, J. Y. Hong, W. A. Goddard, H. Kim, K. Kang, *J. Am. Chem. Soc.* 2013, 135, 9733-9742.

22. S. Novoselov, A. K. Geim, S. V. Morozov, D. Jiang, Y. Zhang, S. V. Dubonos, I. V.

Grigorieva, A. A. Firsov, *Science* 2004, 306, 666-669.

23. J. W. Bai, X. Zhong, S. Jiang, Y. Huang, X. F. Duan, *Nat. Nanotechnol.* 2010, 5, 190-194.

24. Y. X. Xu, K. X. Sheng, C. Li, G. Q. Shi, *ACS Nano* 2010, 4, 4324-4330.

25. W. S. Hummers, R. E. Offeman, *J. Am. Chem. Soc.* 1958, 80, 1339-1340.

26. E. Yoo, J. Nakamura, H. S. Zhou, *Energy Environ. Sci.* 2012, 5, 6928-6932.

27. J. Xiao, D. H. Mei, X. L. Li, W. Xu, D. Y. Wang, G. L. Graff, W. D. Bennett, Z. M. Nie, L. V. Saraf, I. A. Aksay, J. Liu, J. G. Zhang, *Nano Lett.* 2011, 11, 5071-5078.

28. Z. L. Wang, D. Xu, J. J. Xu, L. L. Zhang, X. B. Zhang, *Adv. Funct. Mater.* 2012, 22, 3699-3705.

29. E. Yoo, H. S. Zhou, *ACS Nano* 2011, 5, 3020-3026.

30. Y. C. Lu, B. M. Gallant, D. G. Kwabi, J. R. Harding, R. R. Mitchell, M. S. Whittinghamd, S. H. Yang, *Energy Environ. Sci.* 2013, 6, 750-768.

31. R. Black, S. H. Oh, J. H. Lee, T. Yim, B. Adams, L. F. Nazar, *J. Am. Chem. Soc.* 2012, 134, 2902-2905.

32. R. Younesi, M. Hahlin, M. Treskow, J. Scheers, P. Johansson, K. Edstrom, *J. Phys. Chem. C* 2012, 116, 18597–18604.

33. R. Younesi, M. Hahlin, F. Bjorefors, P. Johansson, K. Edstrom, *Chem. Mater.* 2013, 25, 77–84.

34. S. Meini, N. Tsiouvaras, K. U. Schwenke, M. Piana, H. Beyer, L. Lange, H. A. Gasteiger, *Phys. Chem. Chem. Phys.* 2013, 15, 11478-11493.

35. A. J. Burggraaf, *J. Memb. Sci.* 1999, 155, 45.

36. D. S. Yang, A. H. Zewail, *Proc. Natl Acad. Sci. USA* 2009, 106, 4122-4126.

37. Y. Zheng, C. L. Su, J. Lu, K. P. Loh, *Angew. Chem. Int. Ed.* 2013, 52, 8708-8712.

38. P. Wernet, D. Nordlund, U. Bergmann, M. Cavalleri, M. Odelius, H. Ogasawara, L. A. Naslund, T. K. Hirsch, L. Ojamae, P. Glatzel, L. G. M. Pettersson, A. Nilsson, *Science* 2004, 304, 995-999.

39. O. Leenaerts, B. Partoens, F. M. Peeters, *Phys. Rev. B* 2008, 77, 125416.

40. F. Mehmood, R. Pachter, W. J. Lu, J. Boeckl, *J. Phys. Chem. C* 2013, 117, 10366-10374.

41. H. J. Yan, B. Xu, S. Q. Shi, C. Y. Ouyang, *J. Appl. Phys.* 2012, 112, 104316.

42. W. M. Dose, S. W. Donne, *J Power Sources* 2013, 221, 261-265.

Chapter 7 Conclusion

By engineering the morphology of silicon materials such as tuning the porosity of the nanowires and making hybrid structures, we are capable of making highly efficient and stable silicon photocatalysts. By loading platinum nanoparticles onto the surface of the porous silicon nanowires, we have achieved enhanced performance in photoactivity. To protect the silicon from being oxidized, a silicon/graphene hybrid structure is developed. The enhanced photoactivity and robust photostabilty of the silicon/graphene hybrid structure are attributed to the more efficient photoexcited charge separation on the silicon nanowires, and its subsequent result on avoiding the self-oxidation on silicon nanowires surface during photocatalytic dye degradation. These studies not only open up more opportunities in the application of silicon based solar light harvesting photocatalysts and photoelectrodes, but also provide new insights in the stabilization of other unstable photocatalyst systems.

For the energy storage, we have investigated the modified silicon, silicide family and lithium as anode materials in the air battery systems. Importantly, it is the very first time that silicon and the family of silicide materials are reported as anode materials in the aqueous air battery systems. The assembled silicon battery exhibits an average working potential between 0.9 to 1.2 V at variable discharge current densities. Polarization/galvanostatic measurements and corrosion studies show that a high concentration of the alkaline electrolyte can result in a higher output potential but with more severe corrosion. At a diluted alkaline concentration (0.6 M KOH), specific capacities as high as 1206.0 mA·h/g are achieved. For silicide air battery, several intrinsic features of silicide materials including high electron capacity, high conductivity, high operating voltage, high earth abundance and environmental benignity make them an attractive

class of materials for energy storage. We show that a series of silicide anodes exhibit excellent electrochemical performance with unparalleled capacity. We further define gravolumetric energy density (the product of gravimetric and volumetric energy densities) as a new figure-of-merit to simultaneously characterize the energy density in both gravimetric and volumetric scales. With this new figure of merit, our un-optimized silicide system offers substantial combined advantages over other currently more mature energy storage technologies, with the projected gravolumetric energy density of the $TiSi_2$–air system more than 3–10 times better than that of zinc–air or aluminum–air systems.

The graphene water-resistive membrane Li-air battery we have developed features a highly interconnected graphene network for efficient charge transport, a hierarchical porous structure for efficient diffusion of oxygen and electrolyte ions, a large specific surface area for high capacity storage of insulating discharge product, and a network of highly tortuous hydrophobic channels for generating O_2/H_2O selectivity and effectively retarding moisture diffusion to ensure excellent charge/discharge cycling stability under ambient conditions. It achieves a highest cathode capacity exceeding > 5700 mAh/g (up to 20 cycles) and excellent recharge cycling behaviour (>100 cycles at 1400 mAh/g, and >2000 cycles at 140 mAh/g). Together, the graphene membrane air cathode delivers a lifespan capacity of 110,000-300,000 mAh/g, comparable to that of typical lithium ion battery cathode. Lastly, we further demonstrate that the graphene membrane cathode delivers an exceptional single discharge capacity >18,000 mAh/g, about 100 times higher than cathode capacity of Li-MnO_2 primary batteries. The discovering and exploration of these new air battery systems (silicon-air, silicide-air, Li-air) could offer exciting and attractive high energy density storage alternatives for future mobile power supply.